

## The Impact on Simulated Storm Structure and Intensity of Variations in the Mixed Layer and Moist Layer Depths

EUGENE W. MCCAUL JR. AND CHARLES COHEN

*Universities Space Research Association, Huntsville, Alabama*

(Manuscript received 23 April 2001, in final form 3 January 2002)

### ABSTRACT

The sensitivities of convective storm structure and intensity to variations in the depths of the prestorm mixed layer, represented here by the environmental lifted condensation level (LCL), and moist layer, represented by the level of free convection (LFC), are studied using a three-dimensional cloud model containing ice physics. Matrices of simulations are generated for idealized environments featuring both small and large LCL = LFC altitudes, using a single moderately sheared curved hodograph trace in conjunction with convective available potential energy (CAPE) values of either 800 or 2000 J kg<sup>-1</sup>, with the matrices consisting of all four combinations of two distinct choices of buoyancy and shear profile shape. For each value of CAPE, the LCL = LFC altitudes are also allowed to vary in a separate series of simulations based on the most highly compressed buoyancy and shear profiles used for that CAPE, with the environmental buoyancy profile shape, subcloud equivalent potential temperature, subcloud lapse rates of temperature and moisture, and wind profile held fixed. Two other special simulations, one for each CAPE, are conducted using the high LFC and the lowered LCL, with a neutrally buoyant environmental thermal profile specified in between, such that the equivalent potential temperature was similar to that at the LCL. These latter two cases correspond to situations where the moist layer depth exceeds that of the mixed layer, whereas in all the other cases the two depths were equal.

Results show that for the CAPE-starved environments (CAPE = 800 J kg<sup>-1</sup>) the simulated storms are supercells that are generally largest and most intense when LCL = LFC altitudes lie in the approximate range 1.5–2.5 km above the surface. The simulations show similar trends for the shear-starved (CAPE = 2000 J kg<sup>-1</sup>) environments, except that a tendency toward outflow dominance and multicell morphology is more evident when the LCL = LFC is high. For choices of LCL = LFC height within the optimal 1.5–2.5-km range, peak storm updraft overturning efficiency may approach 100% relative to parcel theory, while for lower LCL = LFC heights, overturning efficiency is reduced significantly. The enhancements of overturning efficiency with increasing LFC height are shown to be associated with systematic increases in both updraft effective diameter and the mean equivalent potential temperature of the low-level updraft, which reaches a maximum near the LFC. For the shear-starved environments, the tendency for outflow dominance is eliminated, but a large overturning efficiency maintained, when a low LCL is used in conjunction with a high LFC. The result regarding outflow dominance at large LCL derives from enhanced evaporation of precipitation in the deeper and drier subcloud layer, but the beneficial effect of a high LFC on convective overturning efficiency, at first glance surprising, derives from the enhanced depth of the moist layer containing the maximum CAPE. The importance of the moist layer depth is highlighted in tests that show that high-LFC storms simulated in environments where the neutrally buoyant sub-LFC layer contains a layer of reduced equivalent potential temperature experience a corresponding decrease in updraft strength. The simulation findings presented here appear to be consistent with statistics from previous severe storm environment climatologies, but provide a new framework for interpreting those statistics.

### 1. Introduction

Early parameter space studies of simulated convective storms focused on major issues such as the effects of bulk convective available potential energy (CAPE) and shear on storm morphology and intensity (Weisman and Klemp 1982, 1984). In those studies CAPE variations were generated using different amounts of low-level water vapor in conjunction with a constant, analytically

specified thermal profile. As a result, the profiles used in those studies featured inextricable linkages between variations in bulk CAPE and variations in the altitudes of maximum parcel buoyancy, the level of free convection (LFC) and the lifted condensation level (LCL).

McCaul and Weisman (2001, hereinafter called MW01) introduced a new method of generating analytical environmental profiles of thermodynamic and kinematic variables for use in initializing cloud models. The new method allows independent specification of bulk CAPE, hodograph trace, the shapes of the buoyancy and shear profiles, the LCL and LFC altitudes, and the moisture profile. The utility of this method was dem-

---

*Corresponding author address:* Eugene W. McCaul Jr., Institute for Global Change Research and Education, 4950 Corporate Drive, Suite 200, Huntsville, AL 35806.  
E-mail: mccaule@space.hsv.usra.edu

onstrated in MW01 in a parameter space study of the effects of buoyancy and shear profile shape on convective storms. The profile shape effects were shown to be profound, with compression of either the buoyancy or shear into the lower troposphere being capable of providing significant compensation for the otherwise expected weakening of storms in CAPE- or shear-starved environments, respectively. Rigorous study of these effects would have been difficult without the capability of enforcing constancy of all environmental parameters except buoyancy and shear profile shape.

MW01 also mentioned that sensitivity tests had shown that systematic variations in the LFC and LCL heights also had considerable impact on simulated storms. It is not entirely obvious how storms might respond to these parameters. McCaul and Weisman (1996) presented simulations that showed that in certain small CAPE environments, storms were most intense when their parcel buoyancy profiles reached maxima in the lower troposphere, with the extra intensity apparently associated with perturbation pressure gradient accelerations produced by strong low-level buoyancy interacting with strong low-level shear. The results of MW01 were consistent with this, in the context of a more general parameter space study conducted using fixed choices for LCL and LFC heights. Because increasing the LFC height, for a fixed buoyancy profile shape, requires an increase in the altitude of maximum buoyancy and attendant upward displacement of buoyancy away from the surface, such LFC increases might act to limit storm intensity under some circumstances. In addition, increases in the LCL heights would be expected to augment subcloud evaporative potential (Braham 1952; Fujita 1959) and surface outflow, and might thereby further prevent storms from developing their full potential intensity. On the other hand, LCL heights are often approximately equal to the depth of the commonly observed well-mixed subcloud layer. This suggests that increases in the LCL height, for fixed subcloud equivalent potential temperature  $\theta_e$ , are accompanied by increases in the depth of the most unstable CAPE (MUCAPE) layer, with attendant reductions in opportunities for updraft dilution by low  $\theta_e$  air and possible benefits for storm intensity.

The purpose of this paper, therefore, is to explore and describe this sensitivity of storms to mixed and moist layer depths, using a detailed cloud model initialized with a series of basic LFC and LCL configurations. Results will be provided for small and large CAPE environments having a moderately sheared curved hodograph suitable for studying the transition between supercell and multicell behavior. The basic simulation experiments are designed such that the depth of the moist layer containing enhanced  $\theta_e$  (the MUCAPE layer) is always represented by the LFC height, so that when we discuss the impact of LFC heights, we are actually using the LFC as a proxy for moist layer depth. Likewise, our LCL heights are always synonymous with mixed layer

depths. In our experiments, we deal only with cases where the LCL is less than or equal to the LFC, other cases being physically unrealizable. Within this context, our data will show that not only do storms tend to become outflow-dominated (see Weisman and Klemp 1982; Brooks et al. 1994a,b; Gilmore and Wicker 1998 for background discussions related to this concept) when LCLs are high, an expected result, but also that updraft effective diameter and overturning efficiency (the ratio of actual peak updraft speed in a simulation to  $(2\text{MUCAPE})^{1/2}$ ) both decrease markedly with decreasing LFC height, particularly when the LFC is less than 1.5 km above the surface. Furthermore, we also show that use of a high LFC in combination with a low LCL leads to strong, persistent updrafts that are less vulnerable to outflow domination.

## 2. Methodology

We construct our idealized environmental profiles using the analytical profile shape function described in the appendix of MW01. This function consists of the scaled product of linearly increasing and exponentially decreasing functions of altitude above a prespecified LFC. For example, our buoyancy profile  $b(z')$  is given by

$$b(z') = E \frac{m^2}{H^2} z' \exp\left(-\frac{m}{H} z'\right), \quad (1)$$

where  $z'$  is altitude above the LFC or some other preselected altitude,  $E$  is a specified CAPE,  $H$  is a vertical scale, and  $m$  is a profile compression parameter. As in MW01, we have  $E = 800$  or  $2000 \text{ J kg}^{-1}$ ;  $H = 14.5 \text{ km}$ ; and, for the low-LCL cases, pressure, temperature, and dewpoint at model level  $k = 2$  of 965 hPa,  $23.5^\circ\text{C}$ , and  $23.0^\circ\text{C}$ , respectively. We also specify  $m = 2.9$  or  $7.0$  for the  $E = 800$  cases, and  $m = 2.2$  or  $4.0$  for the  $E = 2000$  cases. The application of (1) to the construction of our wind profiles is as described in the appendix of MW01.

The exponential argument factor  $m$  in (1) represents the extent to which the function maximum is compressed downwards towards  $z' = 0$ . The vertical integral of the function in (1) is a constant, and is independent of the magnitude of the compression coefficient, a fact which facilitates design of varying buoyancy profiles having constant CAPE. As discussed in MW01, an additional rescaling of the function profile is required to deal with profile truncation by a finite-altitude tropopause, and when applied to wind components, to control maximum wind speed. With parcel buoyancy expressed in terms of this function, the only limitation on the choice of compression coefficient is that it not be so large as to imply a superadiabatic lapse rate just above the LFC. For each choice of compression coefficient, the function produces a single maximum, and the altitudes  $Z'_b$  or  $Z'_v$  of the maxima of buoyancy or  $v$  wind,

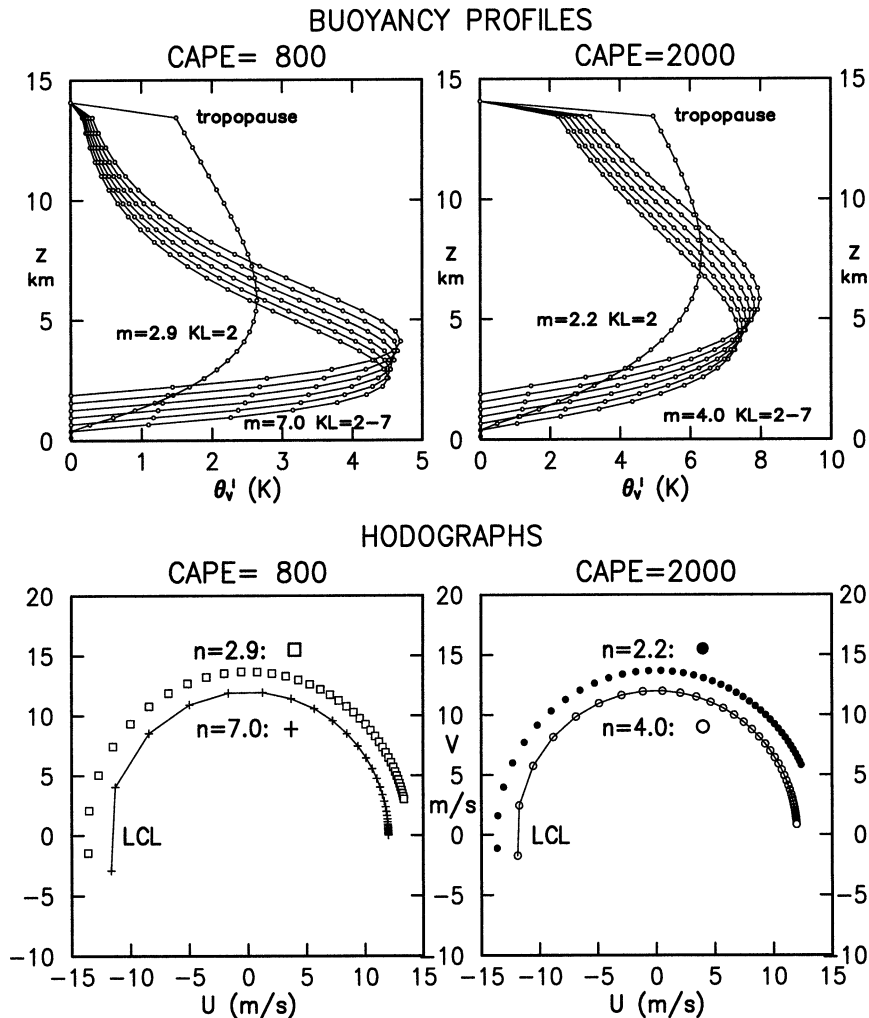


FIG. 1. Shapes of the various buoyancy and wind profiles used in the simulations, with buoyancy expressed in terms of perturbation virtual potential temperature ( $\theta'_v$ ). Left-side panels are valid for the  $\text{CAPE} = 800 \text{ J kg}^{-1}$  simulations, while those on the right side are valid for  $\text{CAPE} = 2000 \text{ J kg}^{-1}$ . Curve parameter  $m$  denotes the value of the profile compression parameter, while KL refers to the model layer nearest the LCL. All buoyancy profiles are truncated by a tropopause at 14-km altitude. Untruncated versions of similarly shaped profiles define the  $v$  wind component in the curved hodograph cases. The shapes of the shear profiles are governed by the value of the profile compression parameter  $n$ . For readability, points on the hodographs are displayed using an unstretched vertical coordinate starting at  $z = 250 \text{ m}$ , with 500-m vertical discretization above, and the hodographs having smaller  $n$  are displaced outward from the nominal  $12 \text{ m s}^{-1}$  radius, whose points are connected with a continuous curve.

respectively, above the LFC, or above our lowest LCL (0.5 km) for wind, are how each profile is identified.

In the experiments described here, we examine environments featuring CAPE values of either 800 or 2000  $\text{J kg}^{-1}$ , and a single semicircular hodograph trace having a radius of  $12 \text{ m s}^{-1}$ . In all our simulations, the ambient tropospheric relative humidity above the LFC is set to 90% relative to either water or ice, as ambient temperatures dictate. In addition, a constant  $\theta_e$  of 354.3 K is specified everywhere in the nearly well-mixed layer below the LCL. Except for the changes in LFC and LCL heights to be studied here, our present experiments cor-

respond exactly in their environmental specifications to those known as E0800-V12C and E2000-V12C in the warm-rain cloud model experiments of MW01. The buoyancy profiles and hodographs used in the present simulations are illustrated in Fig. 1.

In MW01, the LCL and LFC altitudes ( $z_L$  and  $z_F$ , respectively) were always equal and were situated just above the second model level, at an altitude of approximately 0.5 km. For our tests of the impact of variation of LCL and LFC height, we begin with the values of  $z_L = z_F$  from MW01, and systematically raise them one model level at a time, until model level 7 is reached.

This corresponds to an altitude  $z_L = z_F = 2.0$  km. It will be shown later that this range of LCL and LFC altitudes suffices to describe the basic response of storms to LCL and LFC height changes, at least for the exploratory experiments reported here. Additionally, for each CAPE, we have performed one special simulation in which we examine what happens when a high LFC ( $z_F = 1.6$  km) is used in conjunction with a low LCL ( $z_L = 0.5$  km), with a pseudoadiabatic, nearly saturated environmental thermal profile in between. This use of an environmental pseudoadiabatic lapse rate in the layer between the LCL and LFC is necessitated by our desire to ensure that no parcels originating from below  $z_F$  achieve any positive buoyancy until they ascend past  $z_F$ . It also means that the entire layer from the surface up to  $z_F$  is characterized by a constant  $\theta_e$ , and thus constitutes a moist layer that is deeper than the surface-to-LCL layer. The temperature profiles resulting from these specifications are shown on skew  $T$ - $\log p$  charts in Figs. 2a–e. In these figures, the moisture profiles are omitted for clarity.

As we raise  $z_L = z_F$  one model level at a time, we do not change the wind profile, but retain the one from the  $z_L = z_F = 0.5$  km case. Thus, when using our nomenclature to compute the actual altitude of the  $v$  wind component maximum, the height increment that should be added to  $Z'_v$  is only 0.5 km, rather than the variable  $z_L$ . Although in nature any changes in  $z_L$  are often accompanied by changes in the vertical shear associated with boundary layer momentum mixing, we do not allow such changes to our starting environments here. This is done so that we may more rigorously isolate the effects of variations in our initial  $z_L$  or  $z_F$ , without interference by any other corollary environmental changes.

This study employs the Regional Atmospheric Modeling System (RAMS; Pielke et al. 1992; Walko et al. 1995), version 3b, in the same configuration as that used by Cohen (2000), except for domain size and starting data profiles. This nonhydrostatic cloud model solves the fully compressible equations of motion (Tripoli and Cotton 1982) using a time-splitting scheme (Klemp and Wilhelmson 1978), but includes prognostic equations for six species of condensate (rain, hail, graupel, pristine ice, snow, and aggregates) and a diagnostic equation for cloud water mixing ratio. Number concentration is additionally predicted for pristine ice. Subgrid mixing processes are parameterized using the deformation-based scheme of Smagorinsky (1963), with the stability modifications of Lilly (1962). Although the model offers options to evaluate surface fluxes of heat and moisture, these options were not exercised in the present simulations. Boundary layer momentum fluxes were, however, included. A summary of all relevant numerical and physical parameter values used in our version of the model is provided in Table 1. The microphysical parameter values, which determined the size distributions of each particle species, remained the same in all these

parameter-space simulations so as to minimize ambiguity in the interpretation of results.

Based upon our experience and judgment, the RAMS model tended to produce too little anvil ice and too much hail reaching the surface for tropical soundings. To help correct these deficiencies, we made some minor modifications and corrections to the model microphysics. Comparison tests made with the original model show that, while our changes had the desired impact on the microphysics, general patterns in storm structure and intensity were largely unaffected. Thus, we are confident we would have come to the same conclusions about the sensitivities of storms to environmental profile variations regardless of which version of the model we actually used.

One reason the original model produced excessive amounts of hail was related to the fact that mixed-phase particles resulting from collisions were always considered to be ice unless the liquid fraction exceeded 99%. In view of this, we modified the procedure describing mixed-phase collisions such that only the frozen portion of coalesced particles is assigned to an ice category, with the liquid portion shed as rain. As expected, this change decreased the hail mixing ratios, while increasing the rainwater mixing ratios.

In other calculations involving ice particles, it was found that the original RAMS formulation gave erroneously large ice densities for pristine crystals. This problem caused the simulated pristine ice mixing ratios to be too small. To correct this problem, we changed the formula for particle mass  $m$  as a function of diameter  $D$  from  $m = 0.00377D^2$  to  $m = 0.5837D^{2.449}$ , based on an assumed ice density of  $900 \text{ kg m}^{-3}$ , hexagonal plate geometry, and the plate thickness–diameter relationship of Auer and Veal (1970). The exponent we apply to  $D$  above is close to the value recommended by Starr and Cox (1985, their Table B1). This change produced the desired effect of enhanced amplitude of cloud anvil ice mixing ratios.

In these simulations, we use a mesh with 500-m horizontal spacing and total extent 75 km in both directions. Lateral boundaries are open. In the vertical, we use a stretched mesh having spacing of 250 m at the bottom and 750 m at 20-km altitude. Our upper boundary, which lies at 24.5 km, is a rigid lid; the upper 4.5 km of the domain is a Rayleigh friction layer designed to absorb wave motions. For this mesh, we are able to use a large time step of 4.0 s, with five acoustic timesteps between. All simulations are carried out for 120 min, and full model history output files are saved every 5 min for detailed mapping and study.

Starting conditions for all our simulations are horizontally homogeneous, with the exception of the convection-inducing spheroidal thermal bubbles of amplitude 4.0 K or 2.0 K employed for the CAPE = 800 J  $\text{kg}^{-1}$  and 2000 J  $\text{kg}^{-1}$  environments, respectively. The bubbles were centered at  $z = 0$ , and had horizontal radii of 12 km and vertical radii of 2.5 km. These bubble perturbation temperature amplitudes were found to be roughly the smallest that were capable of producing

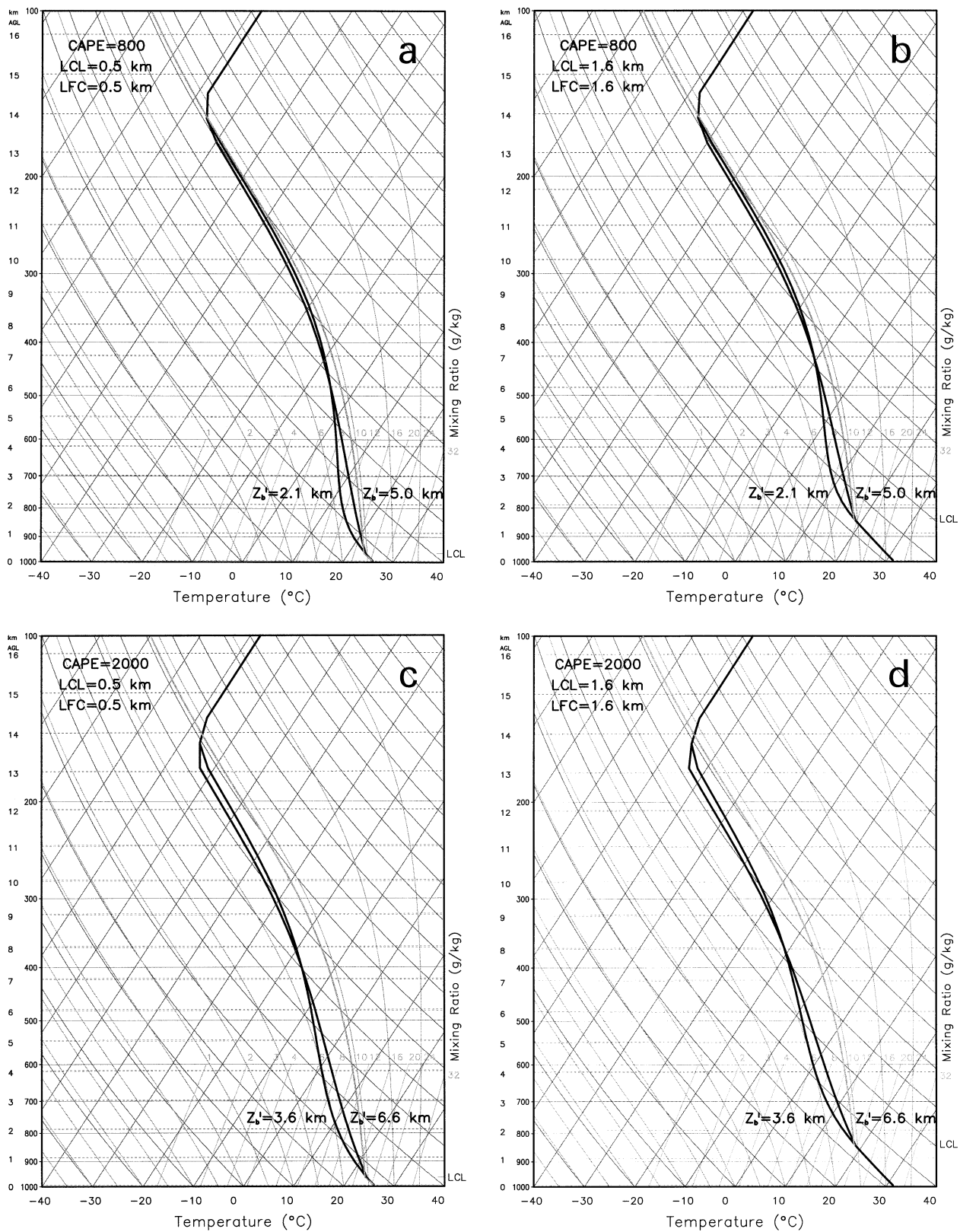


FIG. 2. Skew  $T$  charts of the environmental temperature profiles for (a)  $CAPE = 800 \text{ J kg}^{-1}$ ,  $Z'_b = 2.1$  or  $5.0 \text{ km}$ ,  $z_L = z_F = 0.5 \text{ km}$ ; (b)  $CAPE = 800 \text{ J kg}^{-1}$ ,  $Z'_b = 2.1$  or  $5.0 \text{ km}$ ,  $z_L = z_F = 1.6 \text{ km}$ ; (c)  $CAPE = 2000 \text{ J kg}^{-1}$ ,  $Z'_b = 3.6$  or  $6.6 \text{ km}$ ,  $z_L = z_F = 0.5 \text{ km}$ ; (d)  $CAPE = 2000 \text{ J kg}^{-1}$ ,  $Z'_b = 3.6$  or  $6.6 \text{ km}$ ,  $z_L = z_F = 1.6 \text{ km}$ ; and (e)  $CAPE = 800 \text{ J kg}^{-1}$ ,  $Z'_b = 2.1 \text{ km}$ ,  $z_L = 0.5$ ;  $z_F = 1.6 \text{ km}$ ; and  $CAPE = 2000 \text{ J kg}^{-1}$ ,  $Z'_b = 3.6 \text{ km}$ ,  $z_L = 0.5$ ;  $z_F = 1.6 \text{ km}$ . Moisture profiles are omitted for clarity.

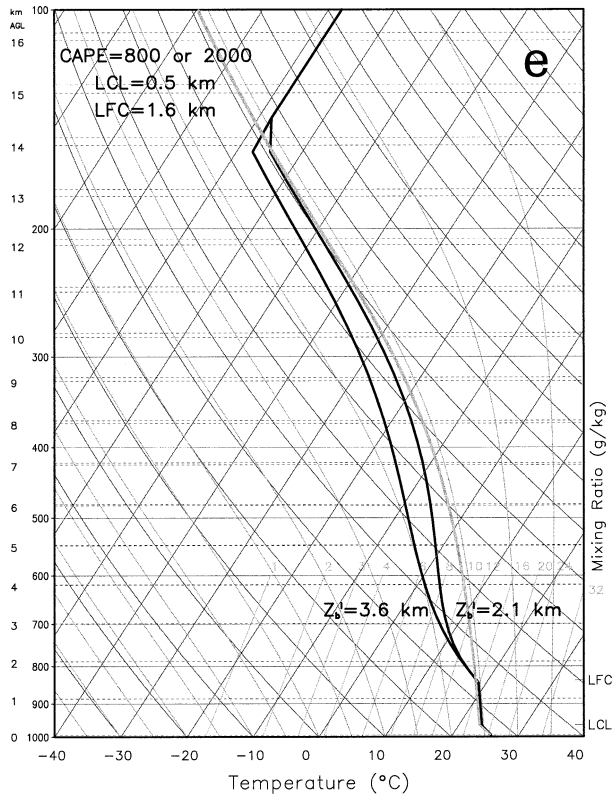


FIG. 2. (Continued)

reasonable-looking storms expeditiously within each simulation matrix.

As a starting point, we first reproduced the E0800-V12C and E2000-V12C simulation matrices of MW01. For all these simulations,  $z_L = z_F = 0.5$  km, which represent relatively low values of LCL and LFC height, as mentioned in MW01. In this paper, we will label these new simulations as E0800-V12C-KL2KF2 and E2000-V12C-KL2KF2, respectively, to reflect the fact that our LCL level  $k_L$  and LFC level  $k_F$  both lie just above model level 2.

In general, we will show, as in MW01, that the largest, most intense storms in these matrices of simulations occur when both the buoyancy and shear profiles are most strongly compressed into the lower troposphere. We therefore use those latter simulations as a foundation upon which to apply changes to  $z_L = z_F$ . The new simulations created by raising the LCL = LFC to model level  $j$  are given the names E0800-V12C-KLjKFj and E2000-V12C-KLjKFj, where the index  $j$  runs from 2 to 7.

After examining simulation results for the varying  $z_L = z_F$  cases, we selected one of the high  $z_L = z_F$  values, namely 1.6 km (just above model level 6), and performed  $2 \times 2$  matrices of simulations for this elevated LCL = LFC that are analogous to the control matrices E0800-V12C and E2000-V12C. These new simulation matrices, named E0800-V12C-KL6KF6 and E2000-V12C-KL6KF6, allow us to see whether the impacts of

TABLE 1. Model numerical and physical parameters.

Parameter	Value
Horizontal resolution $\Delta x, \Delta y$	500 m
Mean vertical resolution $\Delta z$	500 m
Vertical resolution at $z = 0$ $\Delta z_0$	250 m
Vertical resolution at $z = 20$ km $\Delta z_{20}$	750 m
Large time step $\Delta t$	4.0 s
Small time step $\Delta t_s$	0.8 s
Coriolis parameter $f$	0.0 s <sup>-1</sup>
Surface roughness length $z_0$	1.0 cm
Thermal bubble amplitude $\Delta\theta$	2.0 or 4.0 K
Thermal bubble horizontal radius	12.0 km
Thermal bubble vertical radius	2.5 km
Thermal bubble center altitude	0.0 km
Number concentration of cloud droplets $N_i$	300 cm <sup>-3</sup>
Diameter of mean-mass raindrops $D_m$	0.1 cm
Diameter of mean-mass pristine crystals $D_m$	0.1 cm
Diameter of mean-mass aggregates $D_m$	0.1 cm
Diameter of mean-mass graupel $D_m$	0.1 cm
Diameter of mean-mass hailstones $D_m$	0.3 cm
Shape parameter $\nu$ , cloud droplets	1.0
Shape parameter $\nu$ , raindrops	1.5
Shape parameter $\nu$ , pristine crystals	1.0
Shape parameter $\nu$ , aggregates	1.5
Shape parameter $\nu$ , graupel	1.5
Shape parameter $\nu$ , hailstones	1.5

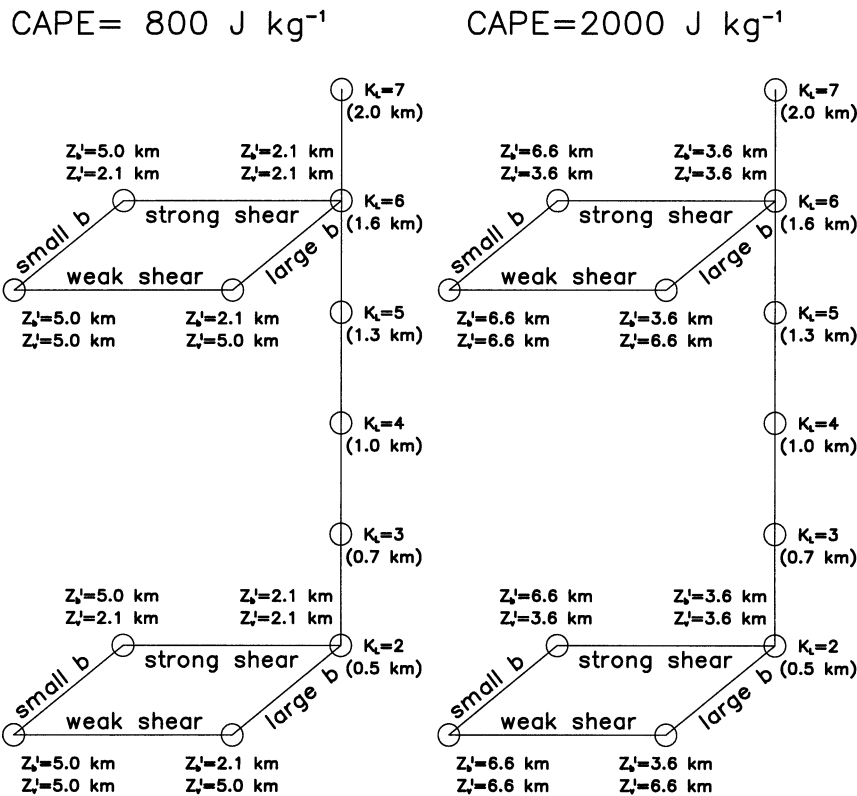
changes to LCL = LFC height show any gross sensitivity to the shapes of either the buoyancy or shear profiles, subject to constancy of the bulk CAPE and hodograph trace. A schematic diagram of the portion of the parameter space embraced by our  $z_L = z_F$  simulations is presented in Fig. 3. No attempt was made in this exploratory study to simulate storms having varying LCL = LFC but lying along the other three ‘‘columns’’ of the parameter space structure shown in Fig. 3.

All the aforementioned simulations were conducted using starting environments characterized by  $z_L = z_F$ , but with systematic changes assigned to  $z_L$  within the columns of simulations, as depicted in Fig. 3. If we visualize these simulations in  $(z_F, z_L)$  space, they all lie along the diagonal, as shown in Fig. 4. The remaining two special simulations, for which  $z_L = 0.5$  km, but  $z_F = 1.6$  km, are represented as off-diagonal data points in Fig. 4. These latter simulations are called E0800-V12C-KL2KF6 and E2000-V12C-KL2KF6. No simulations are possible in the upper-triangular regions of Fig. 4, because of the physical restriction that the LCL never be higher than the LFC.

### 3. Results

We present results from the simulations in various forms. For the  $2 \times 2$  simulation matrices, we present maps of contoured updraft velocity at midlevels, shaded near-surface rainwater mixing ratio, and storm-relative near-surface horizontal wind vectors, for a selected time representative of the mature phase of the principal storm in each simulation. These are constructed in the same way as Figs. 3–4 in MW01, and illustrate several basic aspects of storm size, intensity, and structure.

PARAMETER SPACE SCHEMATIC



Note: wind profiles vary with Z'<sub>v</sub> parameter but are held fixed as K<sub>i</sub> varies

FIG. 3. Schematic design for simulation experiments having equal LCL and LFC altitudes ( $z_L = z_F$ ). Experiments for which  $z_L < z_F$  are not shown here, but are illustrated in Fig. 4. LCL = LFC altitudes are shown in parentheses beneath labels showing the corresponding model level  $k_i$  used in their specification. Here,  $Z'_s$  and  $Z'_v$  represent the altitudes, relative to the LFC and a reference default LFC altitude of 0.5 km, respectively, at which theoretical parcel buoyancy and  $v$  reach their maxima. Here,  $Z'_v$  is taken relative to a default rather than an actual LFC so as to enforce consistency of wind profiles within each column of simulations. However, as the note states, each column, as in MW01, has its own distinct vertical shear profile within the same hodograph trace.

For the columns of simulations having variable LCL = LFC heights (Fig. 3), and for the special simulations where the LFC is higher than the LCL (see Fig. 4), we present not only maps but also time series charts of important structure and intensity parameters associated with the principal simulated storms. In these plots, we will attempt to identify parameters that show strong sensitivity to changes in either LCL or LFC height, or both. In the results that follow, we will have occasion to characterize certain environments as being either CAPE-starved or shear-starved (see also MW01). An environment is said to be CAPE-starved when its bulk CAPE is insufficient to provide an approximately optimal balance against the available bulk shear, to the detriment of mature storm overturning efficiency. Such environ-

ments tend to have bulk Richardson numbers (BRN) smaller than the middle of the supercell range identified by Weisman and Klemp (1982). Likewise, a shear-starved environment is one that has insufficient bulk vertical shear to balance the available bulk CAPE, to the detriment of mature storm overturning efficiency, and perhaps also storm longevity. Shear-starved environments have BRN values larger than that found in the middle of the supercell range.

a. E0800-V12C-KL2KF2 simulations

In Fig. 5 we show for reference the horizontal maps of mature storm structure in the E0800-V12C-KL2KF2 simulation matrix. These RAMS model results may be

LCL vs LFC SCHEMATIC

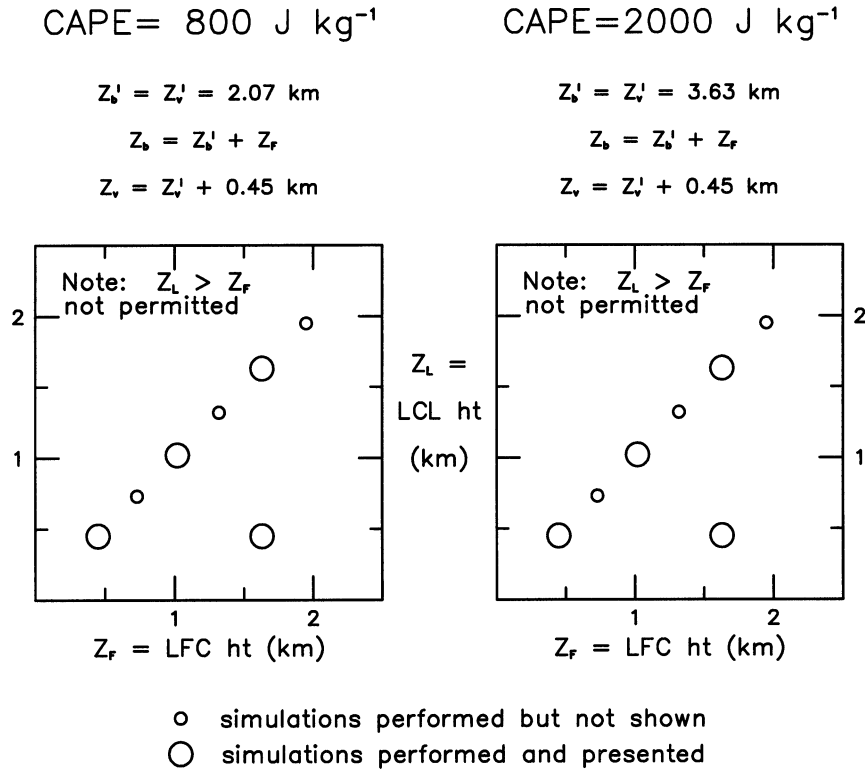


FIG. 4. Schematic design for simulation experiments having LCL altitudes smaller than LFC altitudes ( $z_L < z_r$ ). The diagonal in this diagram corresponds to the large-lapse rate, strong-shear column of experiments in Fig. 3. All experiments shown in each panel feature identical wind profiles, but the wind profiles differ across the two different CAPE values.

compared directly with the warm-rain model results in Fig. 3 of MW01. BRN values for these simulations are as shown in Fig. 5 of MW01, with the upper panels (stronger shear) featuring BRN = 7, and the lower panels (weaker shear) featuring BRN = 17. Based on the findings of Weisman and Klemp (1982, 1984), these environments should support supercell convection. The basic intensity and morphology trends are very similar for the two models, but the structural details and amplitudes of some parameters show differences. In both figures, the weakest storm was the  $Z'_b = 5.0$  km,  $Z'_v = 2.1$  km case (see upper-left panel; note that here  $Z'_b$  is expressed as a distance above the LCL, while  $Z'_v$  is distance above the default LCL altitude of 0.5 km, as noted earlier; in contrast, in MW01, the unprimed quantities  $Z_b$  and  $Z_v$  represented distances above the surface). At the same time, the strongest storm was the  $Z'_b = Z'_v = 2.1$  km case (upper-right panel). Generally, however, the two storms having compressed buoyancy profiles ( $Z'_b = 2.1$  km; right side of each figure) had larger overturning efficiencies than those without. This is consistent with the notion that the particular combination of bulk CAPE and hodograph trace common to all the E0800-V12C-KL2KF2 simulations constituted a CAPE-

starved environment (see MW01). We also find that, because of the inclusion of ice processes in RAMS, the simulated storms are somewhat deeper (not shown) than in the warm-rain model.

*b. E0800-V12C-KL6KF6 simulations*

Figure 6 shows how the CAPE = 800 J kg<sup>-1</sup> storms look when their LCL = LFC heights are increased to 1.6 km, with the environmental wind profiles maintained as in Fig. 5. All the storms are larger and more intense than in Fig. 5. The storm with the largest overturning efficiency occurs in the same matrix position as in Fig. 5, namely the  $Z'_b = Z'_v = 2.1$  km case (upper-right panel), but the peak updraft of the Fig. 6 case is found to be 32 m s<sup>-1</sup>, approximately 50% larger than the 21 m s<sup>-1</sup> seen in the corresponding case from Fig. 5. According to parcel theory, a CAPE of 800 J kg<sup>-1</sup> implies a peak updraft of 40 m s<sup>-1</sup>. Thus, the  $Z'_b = Z'_v = 2.1$  km case in E0800-V12C-KL6KF6 features a remarkably large overturning efficiency of 80%. Some, but not all, of this large overturning efficiency can be attributed to the updraft accelerations associated with the release of the latent heat of fusion in the middle and upper parts

CAPE=0800, V=12, CURVED, LCL=0.5km  
W (Z=1.7 km); QR, WIND (Z=0.1 km)

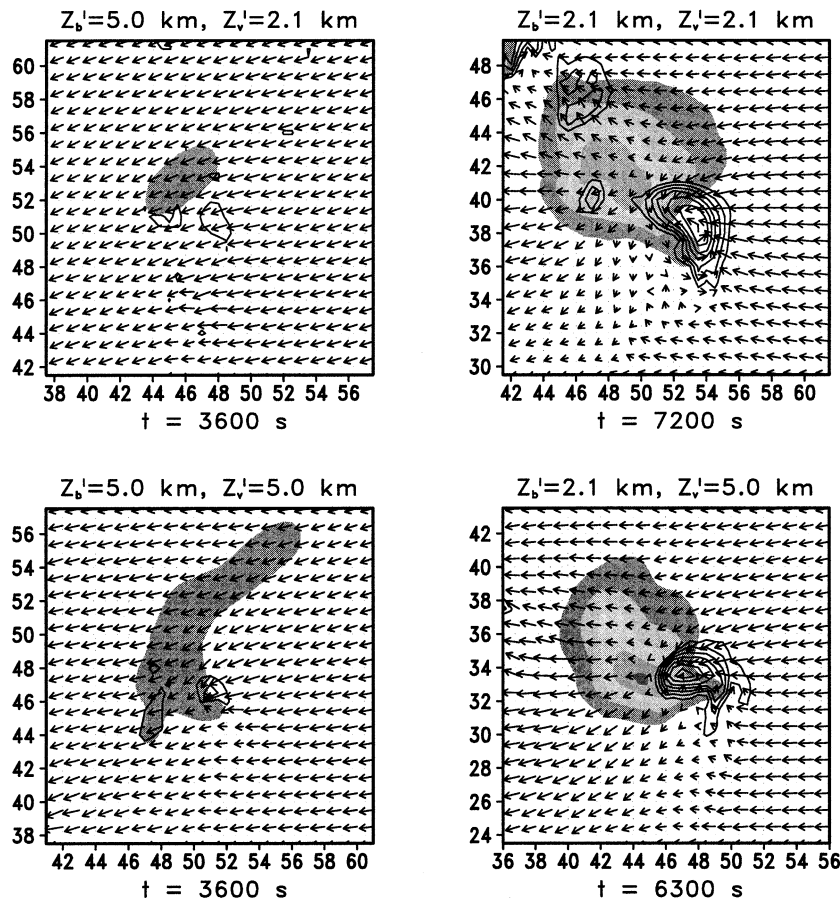


FIG. 5. Maps of simulated updraft velocity  $w$  at  $z = 1.7$  km (contoured at  $2 \text{ m s}^{-1}$  intervals), rainwater mixing ratio  $q$ , at  $z = 0.127$  km (shaded starting at 0.5, 1.0, 2.0, 3.0, and  $4.0 \text{ g kg}^{-1}$  values), and horizontal storm-relative wind vectors (every other vector removed) at  $z = 0.127$  km for the E0800-V12C simulations having  $z_L = z_F = 0.5$  km. Coordinates relative to the full simulation domain are marked at 2-km intervals along the sides of the plots. Vectors are scaled such that a length of 1 km on the plots corresponds to a wind speed of  $12.5 \text{ m s}^{-1}$ . All plots are taken from the second hour of the simulated storms at selected times (see markings beneath each panel) deemed representative of mature storm structure.

of the cloud, effects which are not accounted for in our parcel theory computations. A roughly similar proportional increase in overturning efficiency was found in warm-rain model sensitivity test results, as mentioned in MW01.

Especially interesting in Fig. 6 is the fact that the uncompressed buoyancy profile cases ( $Z'_b = 5.0$  km; see the left two panels of the figure) feature self-sustaining updraft circulations. In contrast, the counterparts of these storms in Fig. 5 (and also in MW01) remained weak or dissipated during the second hour of the simulations.

### c. E2000-V12C-KL2KF2 simulations

Figure 7 contains reference results for the E2000-V12C-KL2KF2 simulation matrix. BRN for the upper

panels (stronger shears) was 29, but was 60 for the lower panels (weaker shears). These values straddle the rough threshold found by Weisman and Klemp (1982, 1984) separating supercell from multicell convection modes, and offer us the opportunity to see what happens in that portion of the parameter space. Although the E2000-V12C results performed for MW01 were not shown there owing to space limitations, we have examined results from both models, and find again that the intensity and morphology trends are essentially the same in both models, but with somewhat stronger, deeper storms in the RAMS simulations. The tendency for storms to be stronger and more supercellular when low-level shears are increased ( $Z'_v = 3.6$  km; see top panels), and for storms to be less intense and more multicellular when shears are reduced, especially when low-level buoyancy

CAPE=0800, V=12, CURVED, LCL=1.6km  
W (Z=3.5 km); QR, WIND (Z=0.1 km)

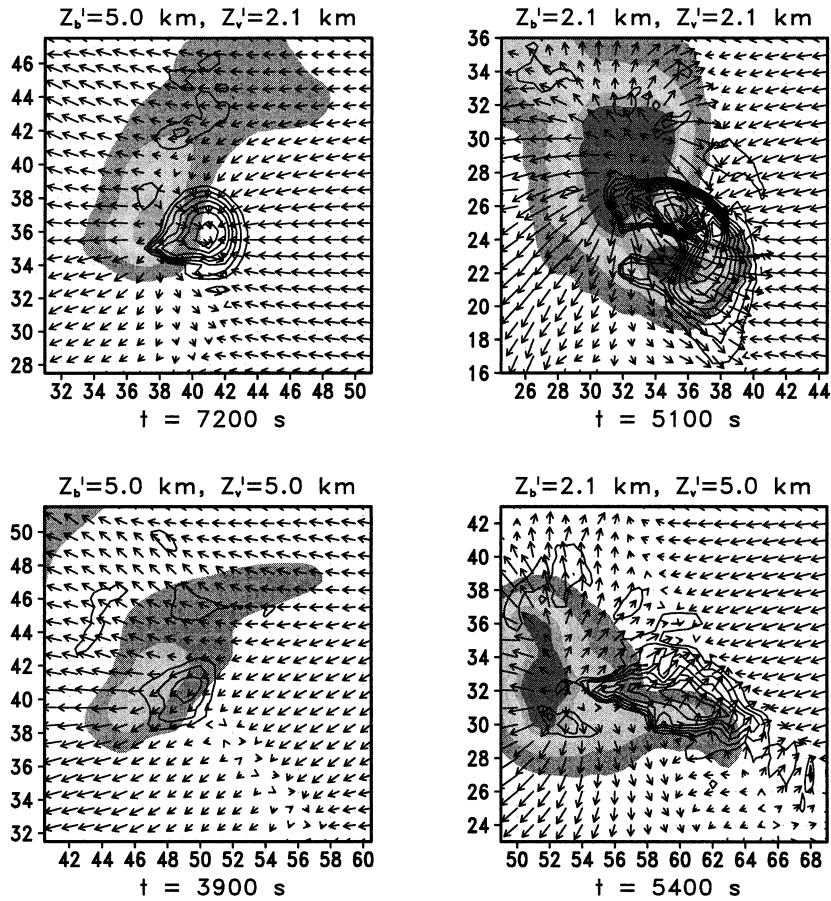


FIG. 6. As in Fig. 5 but for  $z_L = z_F = 1.6$  km, with updraft velocity  $w$  depicted at  $z = 3.5$  km.

is large ( $Z'_b = 3.6$  km), is characteristic of a shear-starved environment (see MW01).

*d. E2000-V12C-KL6KF6 simulations*

When the CAPE = 2000 J kg<sup>-1</sup> storms in Fig. 7 are simulated with their LCL = LFC heights elevated to 1.6 km, the results appear as in Fig. 8. Although all of the storms in Fig. 8 are more intense than those in Fig. 7, most also show signs of outflow dominance and multicellular structure. A storm may be said to be outflow dominated if its surface cold pool spreads out far enough to disrupt or cut off the influx of warm, unstable air into cloud base. This may be reflected in the widespread presence of cold surface air beneath the midlevel updraft, and the absence of warm environmental inflow air there except around the edges of the updraft footprint. Truly outflow-dominant storms tend to degenerate into multicells arranged along an outflow boundary, or to dissipate completely. In contrast, storms that are not

outflow-dominated tend to have at least some undisturbed warm inflow almost directly beneath the main updraft, with attendant benefits to storm organization, intensity, and longevity.

The only real exception to the increasingly multicellular morphological trend seen in comparing Fig. 8 to Fig. 7 is the case with uncompressed buoyancy and enhanced low-level shear,  $Z'_b = 6.6$  km,  $Z'_v = 3.6$  km (see upper-left panel), which appears to be a larger and stronger supercell than its counterpart in E2000-V12C-KL2KF2. Even the storm in the compressed buoyancy and enhanced low-level shear case,  $Z'_b = 3.6$  km,  $Z'_v = 3.6$  km (see upper-right panel), has begun to display multicell structure, although it is not yet fully outflow-dominant. Both of the weak shear cases (see lower panels) are fully undercut by surface outflow by the times the storms reach maturity in terms of updraft development. These LCL-dependent intensity and morphological trends are also consistent with the notion that the basic environment is somewhat shear-starved.

CAPE=2000,  $V=12$ , CURVED, LCL=0.5km  
W ( $Z=1.7$  km); QR, WIND ( $Z=0.1$  km)

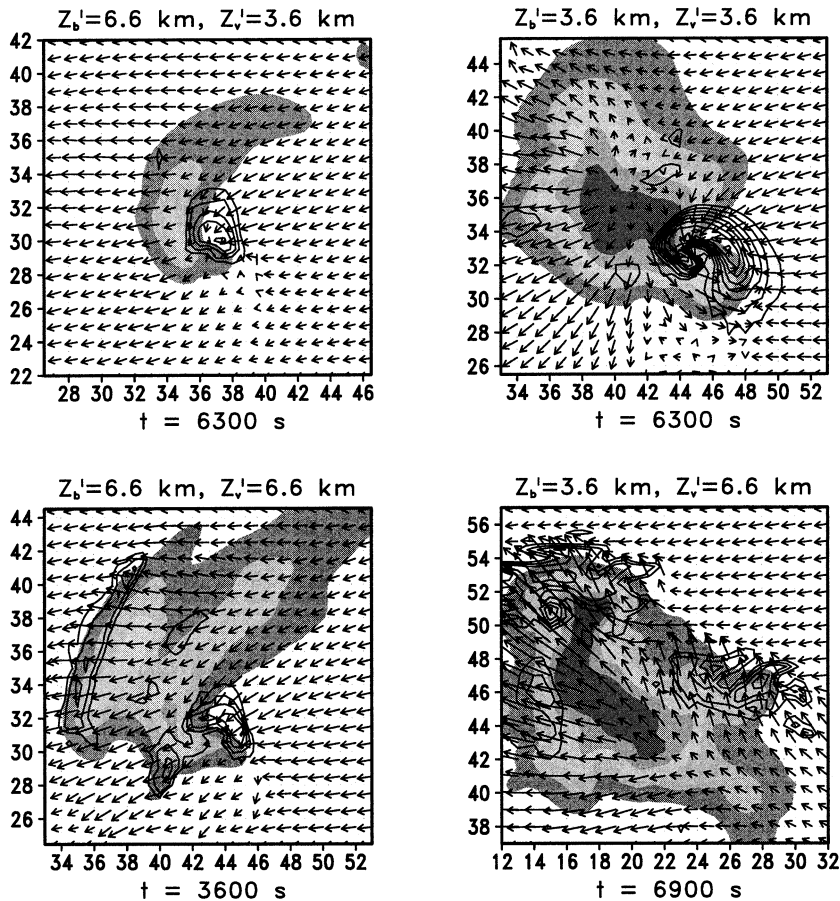


FIG. 7. As in Fig. 5 but for E2000-V12C simulations.

#### e. E0800-V12C-KLjKFk simulations

We now examine in more detail the way in which storm structure and certain key storm intensity and morphology parameters vary as the LCL and LFC are changed, all other aspects of the environment being held fixed. Here, we must generalize our nomenclature, as in the title of this section, because we will begin to consider cases where the LCL may be lower than the LFC. We present results both in map form, as in the previous figures, and also, for key storm intensity and morphology parameters, in time series form. Although many storm intensity and morphology parameters were examined for the time series studies, we present here only the results from a selection of 12 parameters that either exhibited great sensitivity to LCL or LFC height changes, or were considered so basic that their inclusion was warranted, regardless of LCL or LFC height sensitivity.

For simplicity's sake, we present maps (Fig. 9) only from the four simulations having  $k_L = k_F = 2, 4$ , and

6 (i.e.,  $z_L = z_F = 0.5$  km, 1.0 km, and 1.6 km, respectively) and  $k_L = 2, k_F = 6$  (i.e.,  $z_L = 0.5$  km,  $z_F = 1.6$  km). These four simulations, named E0800-V12C-KL2KF2, KL4KF4, KL6KF6, and KL2KF6, are highlighted with extra-wide circles in the schematic diagram of Fig. 4 (left panel). In these maps, the fields presented are analogous to those in Figs. 5–8, with the exception of the updraft field, which is always depicted at 3.5-km altitude, as in Figs. 6 and 8 only.

It is obvious from inspection of Fig. 9 that there is a distinct increasing trend in storm size and intensity as the LCL = LFC altitudes increase from 0.5 km (lower-left panel) to 1.0 km (lower-right panel), and finally to 1.6 km (upper-left panel). These trends are manifest in updraft strength and area, precipitation footprint area and total output, and surface outflow wind speeds. Also noteworthy is the tendency for the surface outflow to occupy more and more of the area under the updraft as the LCL = LFC increases. This can be seen most clearly by examining the wind vectors beneath the stronger por-

CAPE=2000, V=12, CURVED, LCL=1.6km  
 W (Z=3.5 km); QR, WIND (Z=0.1 km)

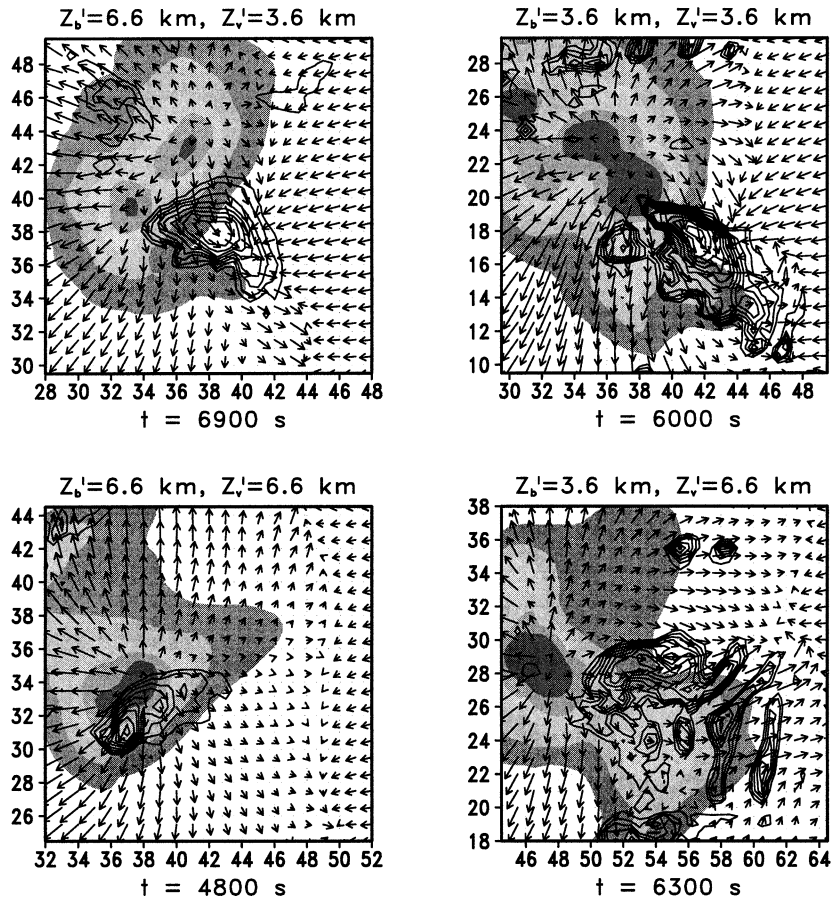


FIG. 8. As in Fig. 7 but for  $z_L = z_F = 1.6$  km, with updraft velocity  $w$  depicted at  $z = 3.5$  km.

tions of the main updraft. Significantly, this trend is reversed for the storm having its LFC at 1.6 km and LCL at 0.5 km (upper-right panel). For this latter storm, the surface outflow winds are confined to the region west of the updraft center, with undisturbed warm inflow air reaching to a point directly beneath the core of the updraft aloft. However, the size and strength of the updraft and precipitation cores for this storm are not very different from those of the LCL = LFC = 1.6 km storm (upper-left panel). All the storms in Fig. 9 display supercell characteristics.

The 12 time series parameters of the principal storms (Fig. 10a-l) include maximum vertical velocity anywhere in the principal storm (WMAX), maximum vertical velocity at 7-km altitude (WMAX7), maximum hail mixing ratio at any altitude (QHMAX), maximum rainwater mixing ratio at any altitude (QRMAX), rainwater footprint area at 0.1-km altitude (QRAREA0), updraft cross-sectional area at 5-km altitude (WAREA5), coldest perturbation potential temperature  $\theta'$  at 0.1-km al-

titude (TMIN0), warmest  $\theta'$  at 0.1-km altitude (TMAX0), maximum ground-relative windspeed at 0.1-km altitude (UVMAX0), maximum vertical vorticity times 10 000 at any altitude (VORTMAX), maximum vertical vorticity times 10 000 at 0.1-km altitude (VORTMAX0), and peak correlation between vertical velocity and vertical vorticity (WVCORR) within the layer between the surface and the altitude of WMAX. Certain updraft-related parameters (WMAX, WMAX7, VORTMAX, VORTMAX0, WVCORR) are assessed using 8-km-wide square box areas centered on the main updraft at 3-km altitude, while midlevel updraft area itself (WAREA5) and precipitation or surface outflow-related parameters are evaluated using 16-km-wide square boxes similarly centered. To reduce the influence of small-scale wave motions, only updrafts exceeding  $2 \text{ m s}^{-1}$  are considered in computing WAREA5. TMAX0, a parameter designed to indicate whether the main updraft is ingesting undisturbed ambient low-level air, is computed using a smaller-sized box region only

CAPE=0800, V=12, CURVED, LCL varies  
W (Z=3.5 km); QR, WIND (Z=0.1 km)

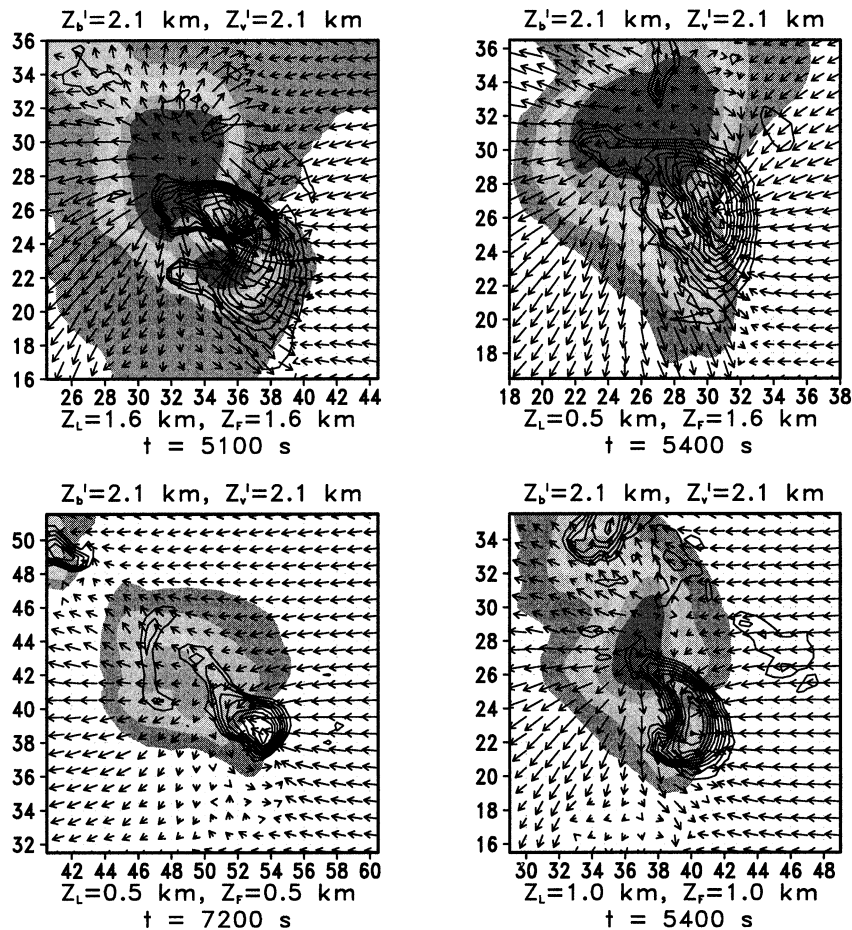


FIG. 9. As in Figs. 5 and 6 but for varying  $z_L, z_F$ .

4-km wide, because the larger boxes were less able to provide distinctive signals for TMAX0.

Fig. 10 contains only time series plots for the simulations mapped in Fig. 9, namely E0800-V12C-KL2KF2, KL4KF4, KL6KF6, and KL2KF6. All time series points are plotted using data from model history files having time resolution of 5 min. As the figure shows, the sensitivity signals are quite strong for most of the 12 key parameters depicted. In addition, the amplitudes of the key parameters tend to show a smooth variation with LCL or LFC height, with rough asymptotic convergence to maximum values as the optimum combinations of LCL and LFC are approached.

In Fig. 10a, WMAX exhibits a clear increasing trend as the LCL = LFC is raised. Peak WMAX for the case when  $z_L = z_F = 0.5$  km is only  $21 \text{ m s}^{-1}$ , while for the case  $z_L = z_F = 1.6$  km, it is  $32 \text{ m s}^{-1}$ . However, WMAX reaches its largest value,  $38 \text{ m s}^{-1}$ , for the case with  $z_L = 0.5$  km,  $z_F = 1.6$  km, although it takes more time for this storm to reach maturity. The convective over-

turning efficiency for the latter case reaches a remarkably large 95% at  $t = 70$  min, but for much of the second hour WMAX for this case is not very different from that of the  $z_L = z_F = 1.6$  km case.

The time series of WMAX7, representing peak updraft speeds at 7-km altitude, are given in Fig. 10b. This altitude is of interest because updraft temperatures are near  $-15^\circ\text{C}$ , where a variety of hydrometeor interactions associated with storm electrification are expected to be present. The trends in WMAX7 as a function of increasing LCL = LFC height are even clearer than for WMAX. Peak WMAX7 for the  $z_L = z_F = 0.5$  km storm is only  $7 \text{ m s}^{-1}$ , while for the 1.0- and 1.6-km storms the peak WMAX7 values are 21 and  $31 \text{ m s}^{-1}$ , respectively. The peak WMAX7 for the  $z_L = 0.5$  km,  $z_F = 1.6$  km storm is  $29 \text{ m s}^{-1}$ , and is roughly the same as for the case where the LCL was also at 1.6 km. The first three cases exhibit differences in WMAX7 large enough and persistent enough to suggest drastic differences in the storms' abilities to generate lightning and

large hail, although this cannot be demonstrated explicitly with our current model. The trends in WMAX7 are approximately mirrored in the time series of simulated hail mixing ratio QHMAX (Fig. 10c), which show mature storm temporal means ranging from zero for the  $z_L = z_F = 0.5$  km storm to 10–15  $\text{g kg}^{-1}$  for both the high-LFC storms. Peak rainwater mixing ratios QRMAX (Fig. 10d) reveal a similar dependence on LFC, but with mean mature-storm mixing ratios ranging only from approximately 8 to approximately 14  $\text{g kg}^{-1}$ .

The variations in near-surface precipitation core footprint area QRAREA0 (Fig. 10e) show many similarities to those of QRMAX, with the high-LFC storms displaying rain areas roughly 50% to 70% larger than those of the low LCL = LFC storm. The  $z_L = 0.5$  km,  $z_F = 1.6$  km storm appears to generate a slightly larger rain core than does the  $z_L = 1.6$  km,  $z_F = 1.6$  km storm, probably because of reduced evaporation associated with its enhanced subcloud relative humidity. Midlevel updraft core areas WAREA5 display similar but even more exaggerated sensitivities (Fig. 10f) than QRAREA0, with the high-LFC storms showing 300% to 400% increases in updraft area compared to the  $z_L = 0.5$  km,  $z_F = 0.5$  km storm. WAREA5 is one of the most sensitive of the morphology parameters that we have identified.

Surface cold pool strength is another parameter of great importance to storm morphology and intensity. Near-surface cold pool potential temperature deficits TMIN0 relative to the environment (Fig. 10g) reveal a strong increasing amplitude trend in TMIN0 as the LCL is raised. For the  $z_L = z_F = 1.6$  km storm, cold pool TMIN0 reaches 9°C, while for the  $z_L = z_F = 0.5$  km storm, TMIN0 never exceeds 3°C. For the  $z_L = 0.5$  km,  $z_F = 1.6$  km storm, TMIN0 is almost indistinguishable from that of the  $z_L = z_F = 0.5$  km storm. Thus, LCL height, not LFC height, is regulating the amplitude of the cold pool TMIN0 in these simulations, when all other key environmental parameters are held fixed. The reader is reminded that all our simulations feature 90% relative humidity above the LFC, so that the influence of variations in midlevel dryness on cold pool strength (see Gilmore and Wicker 1998) is ignored.

The aspects of storm cold pool morphology of greatest importance to storm intensity and evolution are those that lead to outflow dominance, as defined in the previous section. The amplitude of TMIN0 is one way of assessing the strength of the surface cold pool and the likelihood of outflow dominance, but it is not a definitive measure. A better way of studying this issue is to examine our parameter TMAX0, which uses the perturbation potential temperature of the warmest surface air located beneath and near the main updraft core as a measure of the resistance to outflow dominance. In Fig. 10h, we see that for all our CAPE = 800  $\text{J kg}^{-1}$  cases, TMAX0 remains near zero after convection gets underway. This means that none of the storms produces a cold pool large and strong enough to prevent undis-

turbed warm, moist surface air from entering the updraft base. By this measure, none of our 800 CAPE storms are truly outflow-dominated.

Storm cold pools are also frequently associated with strong winds at the surface. The parameter UVMAX0 measures the strength of these winds. As seen in Fig. 10i, this parameter exhibits considerable sensitivity to the LFC height, with UVMAX0 achieving speeds of only 15  $\text{m s}^{-1}$  for the low LCL = LFC storm, but roughly 30  $\text{m s}^{-1}$ , rivalling or exceeding the operational threshold for classification as “severe,” for the two high-LFC storms. Peak UVMAX0 for the  $z_L = 0.5$  km,  $z_F = 1.6$  km storm is actually slightly larger than for the  $z_L = z_F = 1.6$  km storm, but UVMAX0 achieves a larger time-mean value for the latter storm. It should be noted that all the surface wind speeds might have been reduced somewhat if surface heat and moisture fluxes had been included in the simulations, but the relative rankings of the various simulation cases likely would not have changed significantly.

Peak updraft rotation at midlevels is quantified by our parameter VORTMAX (Fig. 10j). For this parameter, clear trends are again evident as the LCL = LFC is raised. VORTMAX grows to roughly 0.02  $\text{s}^{-1}$  for the  $z_L = z_F = 0.5$  km storm and remains rather steady, while for the  $z_L = z_F = 1.6$  km storm, it grows to nearly 0.06  $\text{s}^{-1}$  and exhibits fluctuations. The VORTMAX of the  $z_L = 0.5$  km,  $z_F = 1.6$  km storm never exceeds 0.05  $\text{s}^{-1}$ .

Peak near-surface vorticity is described by the parameter VORTMAX0 (Fig. 10k). This parameter is best thought of as measuring the peak intensity of the storm low-level mesocyclones, and does not necessarily allow inferences to be drawn regarding the important issue of tornado genesis, which our model resolution is too coarse to represent. Despite the inherent noisiness of VORTMAX0, it exhibits trends similar to those of VORTMAX, with the  $z_L = z_F = 1.6$  km storm producing a peak near-surface vorticity greater than 0.06  $\text{s}^{-1}$ . The VORTMAX0 of the  $z_L = 0.5$  km,  $z_F = 1.6$  km storm grows almost as large, but takes more time to do so.

The correlations between vertical velocity and vertical vorticity, WVCORR (Fig. 10l) have often been used to characterize an updraft’s tendency to rotate. Correlations larger than approximately 0.4 usually indicate the presence of sufficient rotation to suggest supercell characteristics, although this is only a rough guideline. Inspection of Fig. 10l shows that, after an initial phase of enhanced correlations ending at around  $t = 60$  min, WVCORR settles down into a quasi-steady pattern during the second hour. During this latter phase, WVCORR is consistently seen to exceed 0.4 for all the storms, with the LCL = LFC = 0.5 km storm having the largest correlations, and the LCL = LFC = 1.6 km storm having the smallest. These patterns are consistent with our other analyses (Fig. 9), which show that all the principal storms tend to be supercellular in our 800 CAPE simulation series.

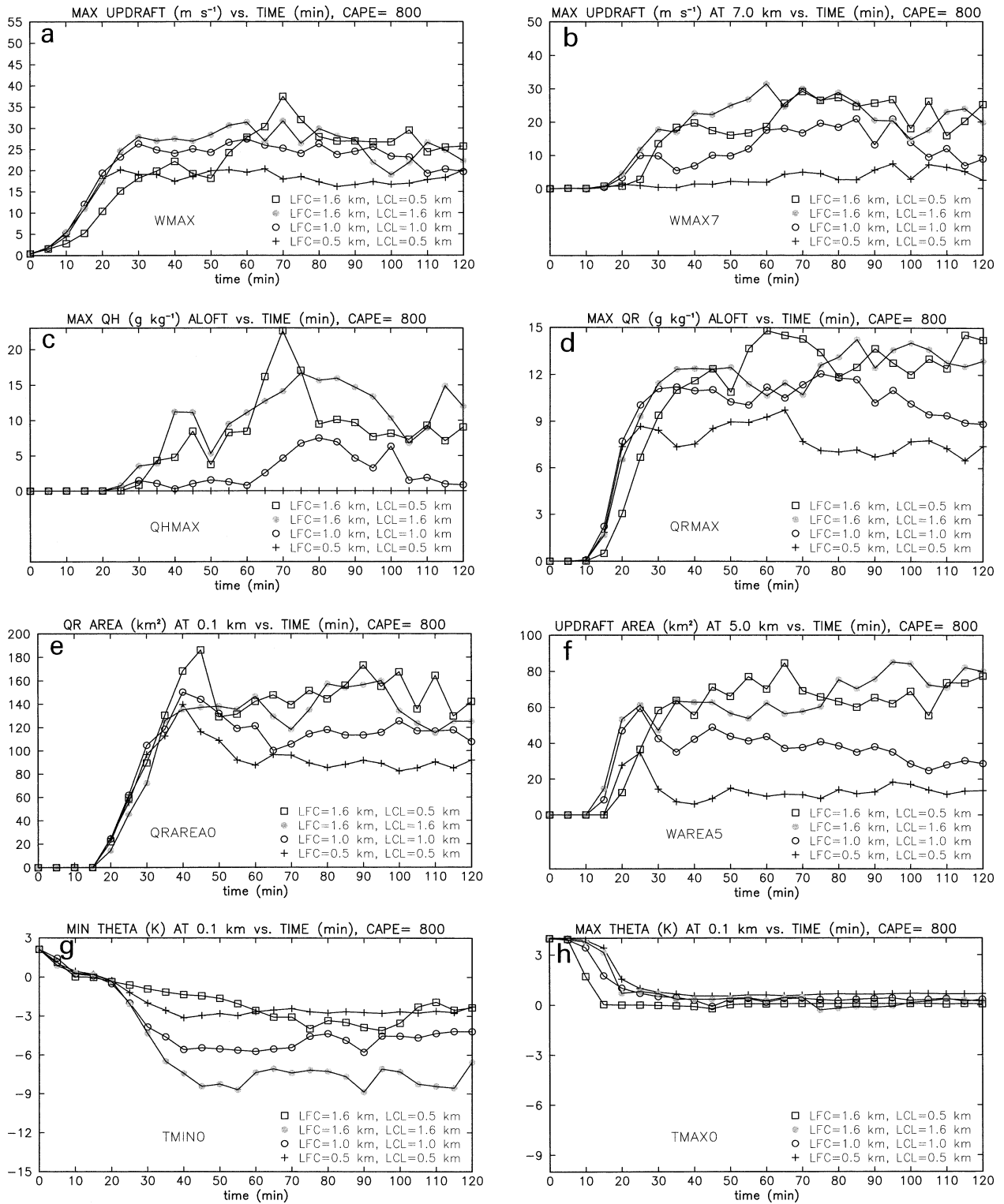


FIG. 10. Time series of key storm morphology and intensity parameters for the E0800-V12C simulations having the following values of LCL and LFC height:  $z_L = z_F = 0.5$  km,  $z_L = z_F = 1.0$  km,  $z_L = z_F = 1.6$  km, and  $z_L = 0.5$ ,  $z_F = 1.6$  km. Each curve is identified by a distinct line type, as shown on each panel. Parameters plotted correspond to those discussed in the text: WMAX, WMAX7, QHMAX, QRMAX, QRAREA0, WAREA5, TMINO, TMAX0, UVMAX0, VORTMAX, VORTMAX0, and WVCORR.

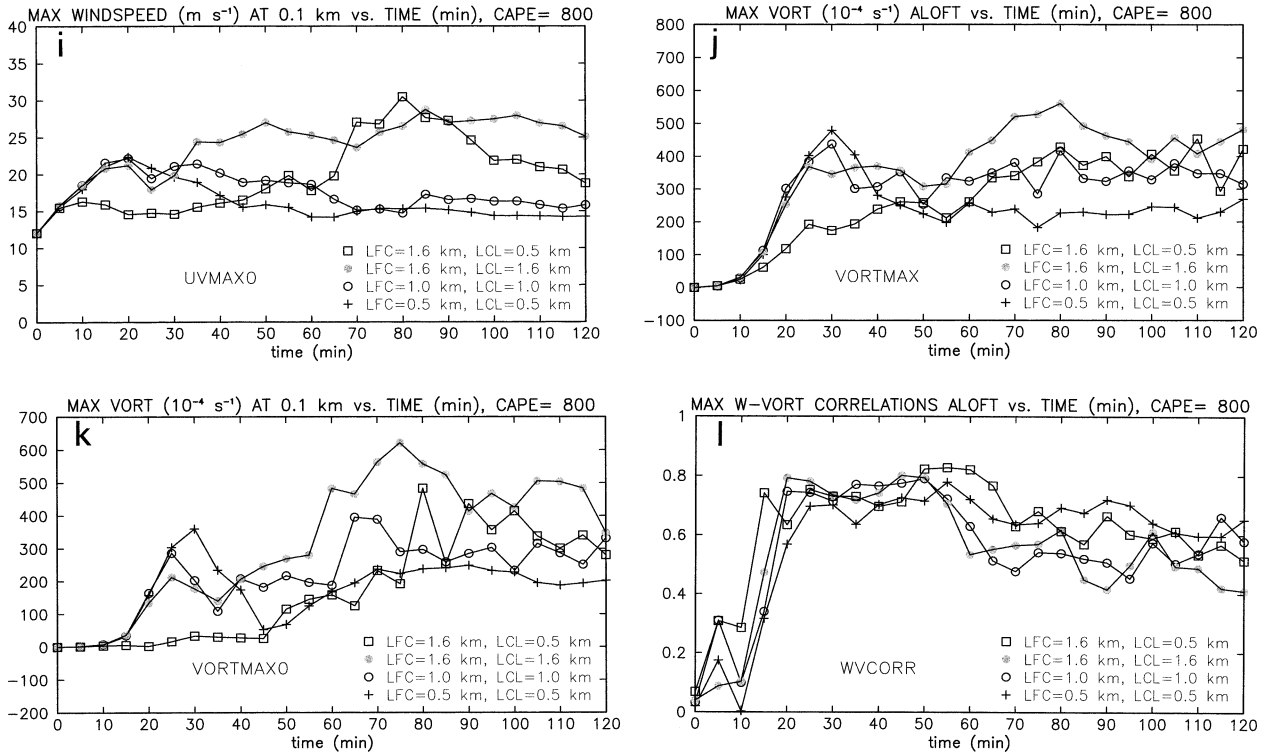


FIG. 10. (Continued)

f. E2000-V12C-KLjKfK simulations

In Fig. 11 we present maps from the four CAPE = 2000 J kg<sup>-1</sup> simulations having  $k_L = k_F = 2, 4$  and 6 (i.e.,  $z_L = z_F = 0.5, 1.0$  km, and 1.6 km) and  $k_L = 2, k_F = 6$  (i.e.,  $z_L = 0.5$  km,  $z_F = 1.6$  km). These simulations are named E2000-V12C-KL2KF2, KL4KF4, KL6KF6 and KL2KF6. The maps in Fig. 11 are analogous to those presented in Fig. 9 for the CAPE = 800 J kg<sup>-1</sup> simulations. The four simulations used in Fig. 11 are highlighted with extra-wide circles in the schematic diagram of Fig. 4 (right panel). The plotting conventions are identical to those for Fig. 9.

In Fig. 11, there is much less evidence of a trend in storm size and strength as the LCL = LFC increases, compared to that seen in Fig. 9. There is, however, a clear trend in storm updraft organization. For instance, the LCL = LFC = 0.5 km storm (see lower-left panel) features a compact, intense supercellular main updraft, while the LCL = LFC = 1.0 km storm (lower right panel) is more elongated and complex in structure, and the LCL = LFC = 1.6 km storm exhibits obvious multicell structural traits. These trends are evidently associated with a tendency toward outflow dominance. The outflow dominance appears most clearly in the LCL = LFC = 1.6 km storm, where the surface outflow is seen to have spread more than 2 km east of the main updraft cores, as well as a similar distance east of the advancing edge of the forward flank precipitation shield. As in Fig. 9, these trends toward outflow dominance and associated

conversion to multicell morphology are largely reversed for the supercell storm having its LFC at 1.6 km and LCL at 0.5 km (upper right panel).

Figures 12a–l depict the time series of key storm parameters and their sensitivities to changes in the LCL and LFC heights for the CAPE = 2000 J kg<sup>-1</sup> cases. All panels of the figures are constructed as in Figs. 10a–l to facilitate intercomparison.

In Fig. 12a, WMAX reveals a clear increasing trend as the LFC increases, echoing the pattern seen in Fig. 10a. In this case, however, the  $z_L = z_F = 0.5$  km storm's largest WMAX reaches 32 m s<sup>-1</sup>, while it soars to nearly 50 m s<sup>-1</sup> for the  $z_L = z_F = 1.6$  km storm. Peak WMAX for the  $z_L = 0.5$  km,  $z_F = 1.6$  km storm is even slightly larger at 54 m s<sup>-1</sup>. At 7 km, peak updraft speeds WMAX7 exhibit similar trends (Fig. 12b), but with less amplitude variation than for WMAX. The cases having LCL = LFC heights near or less than 1.0 km exhibit large losses in WMAX7 amplitude midway through the simulations, followed by recovery and reintensification. These lapses in storm updraft intensity at 7 km are not observed for the high-LFC storms.

Trends in peak hail mixing ratio QHMAX (Fig. 12c) are roughly consistent with those seen for WMAX and WMAX7, but with more temporal variability and overlap of the time series curves. QHMAX in the second hour varies from as little as 1 g kg<sup>-1</sup> to as much as 13 g kg<sup>-1</sup> for the  $z_L = z_F = 0.5$  km storm, but approaches or exceeds 20 g kg<sup>-1</sup> for the high LFC storms. The

CAPE=2000, V=12, CURVED, LCL varies  
W (Z=3.5 km); QR, WIND (Z=0.1 km)

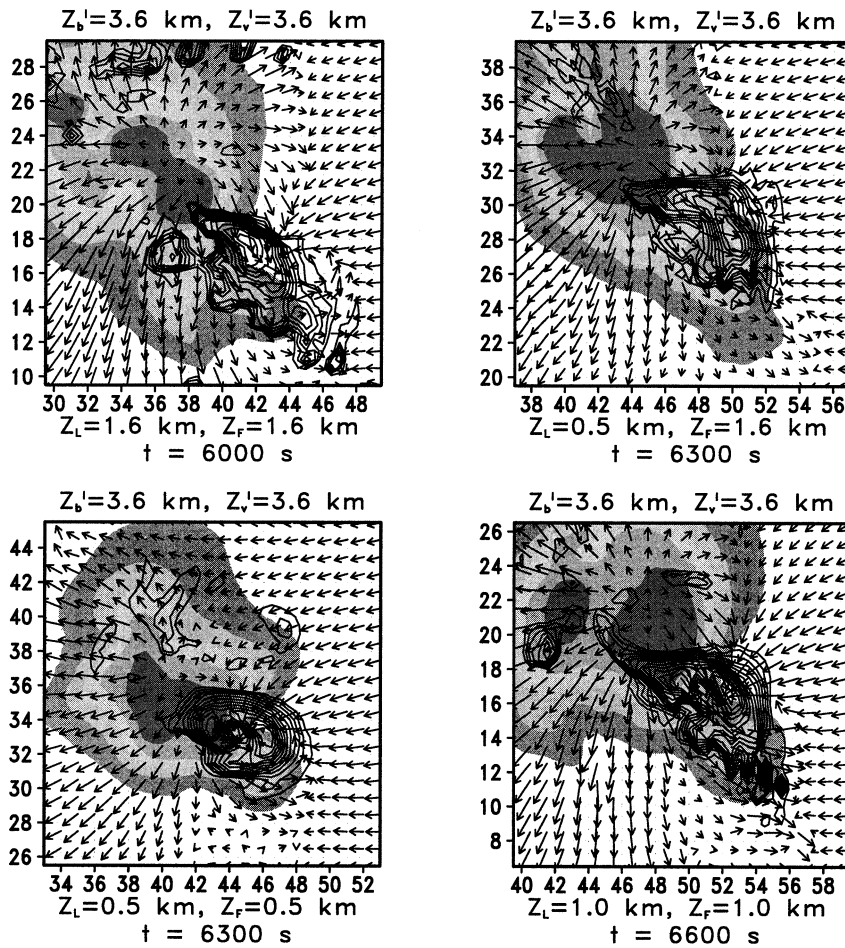


FIG. 11. As in Fig. 9 but for E2000-V12C simulations.

signals in the peak rainwater mixing ratio QRMAX (Fig. 12d) are much more subtle than QHMAX, with all storms showing peak QRMAX values lying in the 10–14  $\text{g kg}^{-1}$  range for much of the second hour. Near-surface rain footprint areas QRAREA0 (Fig. 12e) also reveal only weak trends. There is, however, a tendency for the  $z_L = 0.5$  km,  $z_F = 1.6$  km storm to display the largest QRAREA0, probably because it has the strongest updraft and most intense precipitation core, combined with its enhanced sub-LFC relative humidity and reduced susceptibility to evaporation of precipitation. Midlevel updraft areas WAREA5 (Fig. 12f) show only weak increases in response to increases in LCL height.

The maximum near-surface cold pool potential temperature deficits TMIN0 (Fig. 12g) again show clear increases in amplitude as the LCL increases, reminiscent of the variations seen for CAPE = 800  $\text{J kg}^{-1}$  in Fig. 10g. As in Fig. 10g, the two low-LCL storms are both seen to have peak TMIN0 deficits of only about 4°C,

as opposed to the high-LCL cases, where TMIN0 sometimes reaches 10°C. The TMAX0 parameter (Fig. 12h) reveals much more temporal structure than its counterpart at small CAPE (see Fig. 10h). In particular, the two highest LCL cases exhibit occasional significant loss of access to undisturbed ambient warm surface air, and are thus susceptible to outflow domination. This is especially true during the storm splitting and reorganization that occurs around 1 h into the simulations, but is also observed later in the simulations for the  $z_L = 1.6$  km storm. The susceptibility to outflow dominance is almost entirely eliminated in all the  $z_L = 0.5$  km storms, including the case with  $z_F = 1.6$  km. Peak surface wind speeds UVMAX0 (Fig. 12i) in the second hour are weaker, approximately 20  $\text{m s}^{-1}$ , for the  $z_L = z_F = 0.5$  km storm than for the other storms, which generate winds of 25–30  $\text{m s}^{-1}$ .

Peak midlevel vorticity VORTMAX (Fig. 12j) again reveals only weak trends as the LFC and LCL are

changed. All storms achieve sizable peak VORTMAX values between  $0.05\text{--}0.07\text{ s}^{-1}$  during the second hour of the simulations. Only the  $z_L = z_F = 0.5\text{ km}$  storm shows a tendency to have consistently weaker midlevel rotation than the other storms. At the surface, the picture for VORTMAX0 is substantially more complex (Fig. 12k). All the storms produce peak values of VORTMAX0 varying between  $0.03\text{--}0.05\text{ s}^{-1}$  late in the simulations, and show considerable time series overlap. Interestingly, the data suggest that the  $z_L = z_F = 1.0\text{ km}$  storm may actually achieve the largest VORTMAX0 during the final 30 min of the simulations.

Updraft–vorticity correlations WVCORR (Fig. 12l) resemble those for the 800 CAPE cases, but take somewhat longer to reach their initial peak and settle into a more mature quasi-steady state. During the last 40 min of the simulations, correlations are seen to range from about  $0.3\text{--}0.6$ , or roughly  $0.1$  less than corresponding values seen for the 800 CAPE simulations. Again, the smallest correlations, and greatest tendency toward multicellular structure in the late stage of the simulations (particularly after  $t = 80\text{ min}$ ), are found in the  $LCL = LFC = 1.6\text{ km}$  case. This is consistent with impressions gleaned from Fig. 11.

#### 4. Discussion

##### *a. The mixed layer and moist layer effects*

The general sensitivities to the buoyancy and shear stratification seen in the E0800-V12C-KL2KF2 and E2000-V12C-KL2KF2 simulation matrices (Figs. 5 and 7) are very similar to those reported for the warm-rain-only simulations of MW01. In the present simulations, the amplitudes of many storm intensity parameters are somewhat different and storm top heights are usually larger, but this is not surprising in view of the inclusion of ice physics in the present model. Based on the simulations presented here, we see no reason to modify any of the basic conclusions of MW01. Indeed, the subject of the following discussion, the influence on convection of the mixed and moist layer depths, was first discovered in sensitivity tests of the MW01 results obtained using the warm-rain model of Klemp and Wilhelmson (1978). This gives us considerable confidence that our main storm-scale morphology findings here are indeed robust, and will not change significantly even as numerical models of storms continue to improve in the future.

Comparing the high  $LCL = LFC$  simulations of E0800-V12C-KL6KF6 (Fig. 6) with those of E0800-V12C-KL2KF2 (Fig. 5), it is clear that all the simulated storms at  $CAPE = 800\text{ J kg}^{-1}$  grow larger and more intense when the  $LCL = LFC$  is raised. Based on the data presented here, this pattern of trends does not appear to be strongly dependent on the shapes of the buoyancy and shear profiles; all members of the matrix of simulations in Fig. 6 exhibit roughly comparable increases in intensity when the  $LCL = LFC$  heights are

raised by the same amount. Because these storms exist in an environment that features bulk CAPE and shear values suggestive of moderate CAPE starvation, they benefit from anything that acts to compensate for that CAPE starvation. MW01 and our E0800-V12C-KL2KF2 and E2000-V12C-KL2KF2 simulations demonstrate that one way of compensating for CAPE starvation, without actually boosting CAPE, is to compress the buoyancy into the lower troposphere, so that low-level buoyancies and environmental lapse rates are larger for the specified CAPE. This pattern appears to be important for the development of strong, and possibly tornadic, low-level mesocyclones in landfalling tropical cyclones (McCaul and Weisman 1996). For a given CAPE and buoyancy profile shape choice, another possible way to compensate for small CAPE within the context of our experiments is to raise the LCL and LFC, if they are lower than the optimal. Our Figs. 9 and 11 suggest that LFCs above about  $1.5\text{--}2.0\text{ km}$  are close to optimal; such elevated LFCs tend to boost updraft overturning efficiency relative to lower LFCs. The exploratory simulations presented here suggest that, for cases of CAPE starvation, the LCLs should be near the LFC in order for storms to reap maximum gains in overturning efficiency.

In contrast, comparing the high  $LCL = LFC$  simulations of E2000-V12C-KL6KF6 (Fig. 8) with those of E2000-V12C-KL2KF2 (Fig. 7), most of the large-CAPE storms gain only moderately in intensity when their  $LCL = LFC$  altitudes are raised. This appears true for many of the parameters studied here. These storms exist in an environment that is slightly shear-starved, and thus do not grow significantly larger or more intense under buoyancy profile compression or  $LCL = LFC$  elevation. In fact, the weak-shear, large-lapse-rate case from E2000-V12C-KL2KF2 (see lower-right panel of Fig. 7) already shows evidence of conversion to a multicell form, in contrast to the supercell forms that prevail in the other simulations of E2000-V12C-KL2KF2. Raising the  $LCL = LFC$ , as in E2000-V12C-KL6KF6 (see Fig. 8) exacerbates this multicell tendency; only the small-lapse rate, strong-shear case (see upper-left panel of Fig. 8) sees enhancement of its supercell characteristics, while all the other storms exhibit less purely supercellular, or even obviously multicellular, character. Thus, the  $LCL$ - and  $LFC$ -dependent trends in storm intensity and morphology in the large-CAPE simulations are somewhat different from those seen in the small-CAPE simulations.

While updraft overturning efficiency for all the E2000-V12C-KL6KF6 storms is greater than that for the E2000-V12C-KL2KF2 storms as a result of the changes in LFC heights, the optimal specification of LCL for these slightly shear-starved storms is more difficult to ascertain from the present exploratory simulations. However, in Fig. 11 the results from the large low-level lapse rate, strong low-level shear E2000-V12C-KL2KF6 case (upper right panel) show a slightly

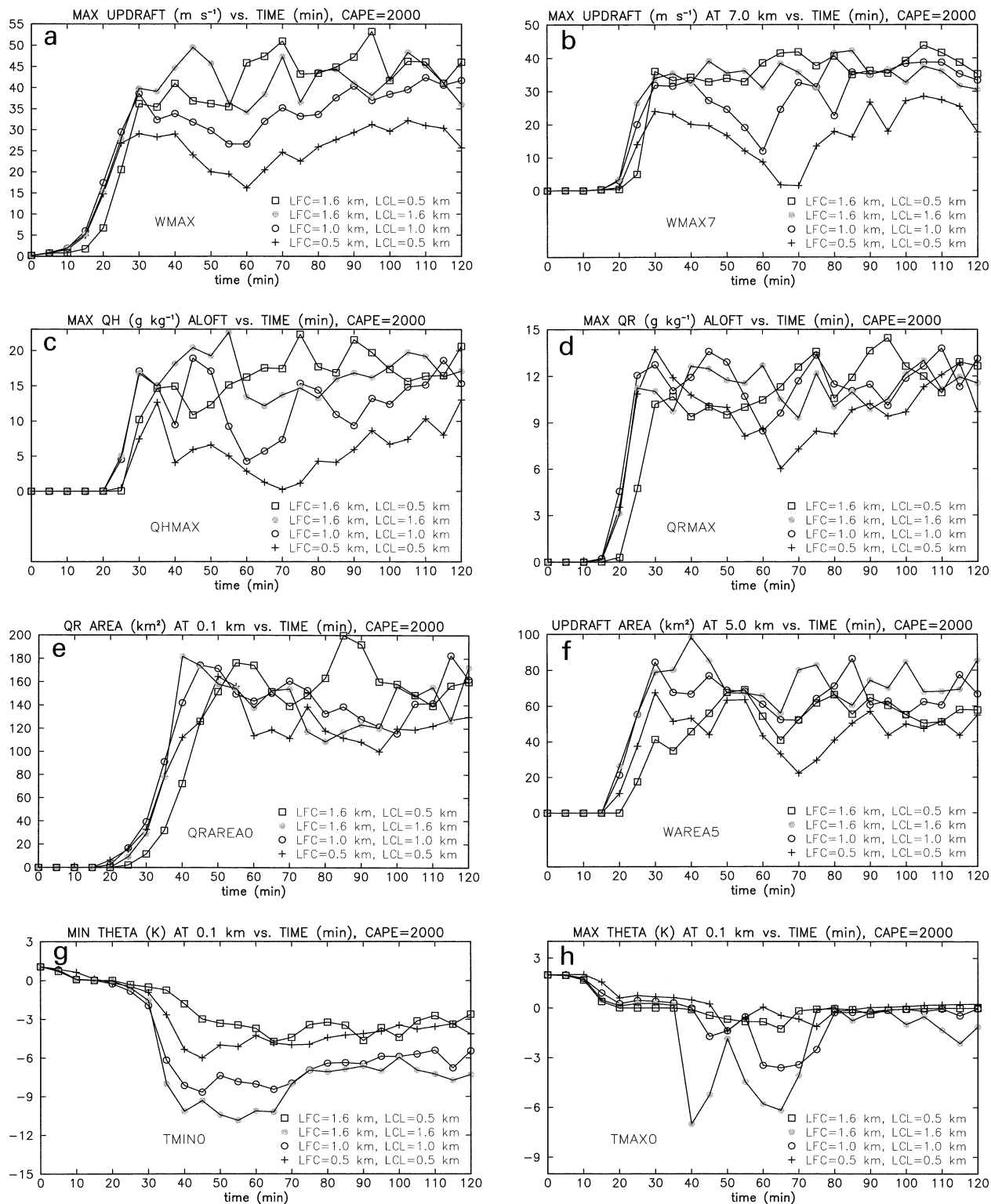


FIG. 12. As in Fig. 10 but for the E2000-V12C simulations.

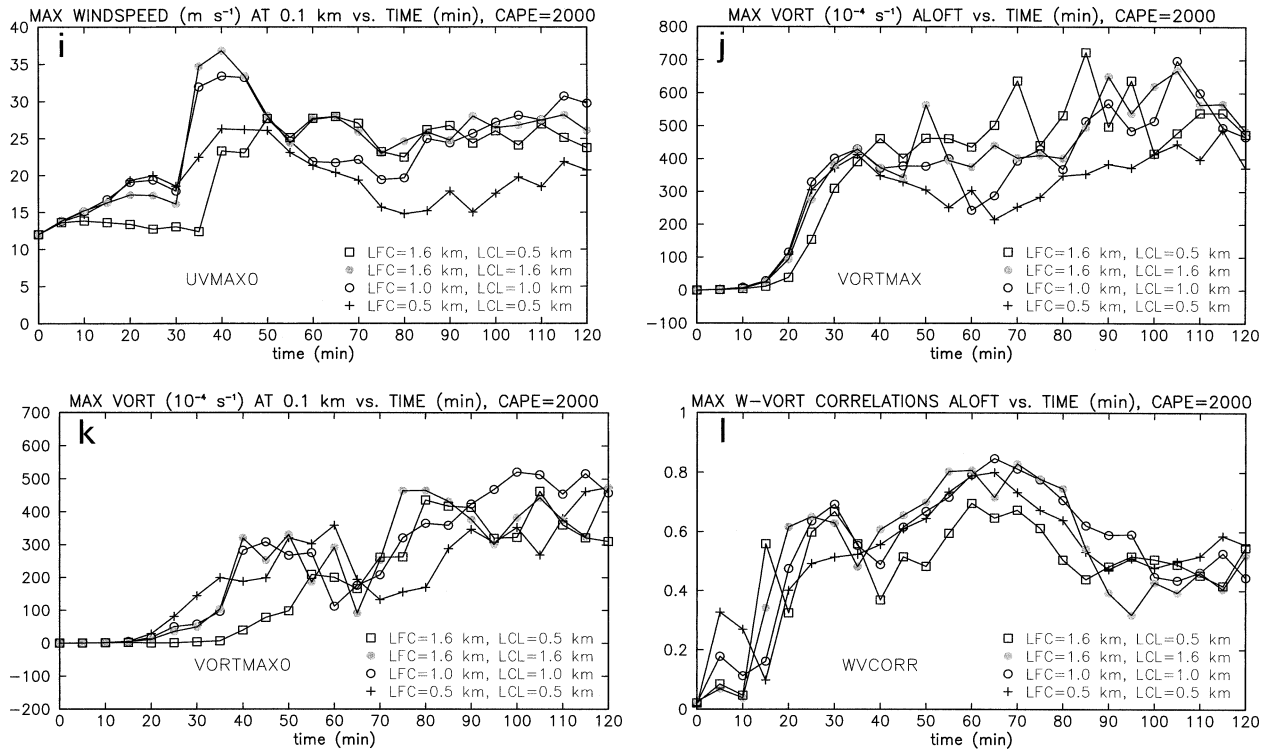


FIG. 12. (Continued)

stronger updraft, greater updraft persistence, larger updraft–vorticity correlations, warmer surface outflow, and less tendency for outflow domination, compared to the companion E2000-V12C-KL6KF6 case. Thus, when CAPE is plentiful relative to the bulk tropospheric shear, storms appear to benefit when excessively cold surface outflows are prevented, as long as a high LFC is retained; within the context of our present study, this can be accomplished either by raising the altitude of maximum buoyancy  $Z'_b$ , or by lowering the LCL to an altitude well below the LFC. The benefits of doing these things appear to hold true for many of the storm parameters discussed here, not just overturning efficiency.

Based on the trends seen in our results, we may clearly distinguish what we call the “moist layer effect” from the “mixed layer effect.” The former is associated with enhancement of updraft size and strength as the LFC height increases (within reasonable limits), as long as there are no substantial minima in  $\theta_e$  in the sub-LFC layer. The moist layer effect appears to be one of the principal direct determinants of overall storm intensity, as reflected in updraft overturning efficiency, rain and hail production, and, in all likelihood, degree of storm electrification. The mixed layer effect, on the other hand, is associated with enhancement of surface cold pool temperature deficits as the LCL height increases and subcloud layer relative humidity decreases. It thus strongly influences the strength of storm surface outflows and thereby exerts its own fundamental controls on storm morphology and persistence.

*b. Effects on storm morphology*

The BRN, because of its simple combination of bulk measures of CAPE and 0–6-km shear, has found wide utility among forecasters in predicting storm type. However, it is also widely recognized that the BRN cannot provide a definite threshold value for the transition between supercell and multicell storms. We believe our results, along with those of MW01, demonstrate some of the factors that allow storms to exhibit a range of morphological types for intermediate values of BRN.

As mentioned earlier, all the strongly sheared storms in our E0800-V12C simulation matrices (upper panels of Figs. 5–6) are associated with BRN = 7, while the weakly sheared storms (lower panels) are associated with BRN = 17. All these storms are, as expected, supercellular, although the high-LCL = LFC case with small  $Z'_b$  and large  $Z'_v$  (lower-right panel) of Fig. 6 is on the verge of becoming multicellular. However, our E2000-V12C simulation matrices (Figs. 7–8) feature BRN values that straddle the supercell–multicell transition, and offer an opportunity to see how storm morphology changes in response to changes in buoyancy profile shape and LCL and LFC altitudes.

In the low LCL = LFC cases of E2000-V12C (Fig. 7), both storms in the more strongly sheared environments (upper panels) have BRN = 29, and display supercell morphology. For the weakly sheared environments (lower panels), where BRN = 60, differences in morphology are apparent. The large  $Z'_b$  storm, with weak

buoyancy in a deep layer (lower-left panel), is a supercell, which is contrary to expectations based on BRN. Meanwhile, the small  $Z'_b$  storm, with buoyancy compressed into the lower troposphere (lower-right panel), is clearly multicellular, more in line with BRN theory.

In the high LCL = LFC cases of E2000-V12C (Fig. 8), the increase in LCL = LFC height has led to additional morphological changes, even though BRN values are identical to those in Fig. 7. For the weakly sheared storms (BRN = 60) in Fig. 8, we see that the small  $Z'_b$  storm, with buoyancy compressed into the lower troposphere (lower-right panel), is again multicellular, as in Fig. 7. However, now the large  $Z'_b$  storm (lower-left panel) has succumbed to outflow dominance, and although still unicellular, finds its updraft positioned fully 10 km away from warm, undisturbed air. This storm thus displays many of the characteristics of a “pulse” storm. Meanwhile, for the strongly sheared cases (BRN = 29), the small  $Z'_b$  storm (upper right panel) retains some supercell characteristics but struggles against outflow dominance and is starting to show multicell character, while the large  $Z'_b$  storm (upper left panel) remains a respectable supercell.

The morphological response of the storms to changes in LCL and LFC may also be appreciated by examining the horizontal cross-section maps in Fig. 9 (CAPE = 800 J kg<sup>-1</sup>) and Fig. 11 (CAPE = 2000 J kg<sup>-1</sup>). In Fig. 9, increases in the height of the LCL = LFC result primarily in larger, stronger supercells. In Fig. 11, however, increases in the LCL = LFC height lead to an increase in storm intensity, but also to an increase in multicell traits. In both figures, but especially for the large CAPE case, reduction of the LCL height under a high LFC leads to a reduction in tendencies for outflow dominance, and to enhancement of supercell character.

### c. Sensitive storm parameters

The time series plots of key storm parameters for the E0800-V12C KL2KF2, KL4KF4, KL6KF6, and KL2KF6 low- $Z'_b$ , low- $Z'_v$  simulations (Fig. 10) show, in most cases, considerable sensitivity to changes in the LCL = LFC heights. In this CAPE-starved environment, parameters WMAX, WMAX7, and WAREA5 exhibit particularly strong sensitivity to the LCL = LFC changes. For most storm parameters, the KL2KF6 storm is only marginally stronger than its KL6KF6 counterpart; neither of these storms was in danger of becoming outflow-dominant, so that modification of the surface cold pool temperature by means of LCL height changes had only minor effects on storm intensity, structure, and persistence.

For the shear-starved E2000-V12C KL2KF2, KL4KF4, KL6KF6, and KL2KF6 low- $Z'_b$ , low- $Z'_v$  simulations, however, most key storm parameters (Fig. 12) showed reduced sensitivity to the specification of the LCL = LFC height. This is attributable to the tendency for these storms to convert from supercell form to mul-

ticell form as surface outflow becomes excessively strong. Such tendencies are also reflected in the general reduction of mature-stage updraft-vorticity correlation amplitudes for the E2000-V12C simulations (Fig. 12) versus those for E0800-V12C (Fig. 10). This morphological transition from supercell to multicell is, however, largely suppressed in the E2000-V12C-KL2KF6 storm, evidently because of its environment's higher subcloud relative humidity and reduced ability to support the strong evaporatively cooled surface outflows seen in the KL6KF6 storm. For this shear-starved environment, parameters WMAX and WMAX7 show the greatest sensitivities to LCL = LFC changes, but they are not as dramatic as those seen in the more strongly CAPE-starved E0800-V12C simulations. It should be noted, however, that the low- $Z'_b$ , low- $Z'_v$  storms in the shear-starved environments are apparently not the ones most sensitive to changes in environmental parameters. Comparison of Figs. 7 and 8 indicates that both high- $Z'_b$  shear-starved cases exhibit sizable increases in updraft size and strength as the LCL = LFC is raised.

The sensitivity of storm updraft area to LFC height, seen to be especially dramatic at CAPE = 800 J kg<sup>-1</sup>, appears to be a major factor in regulating whether supercells in such small-CAPE environments are miniature (McCaul and Weisman 1996) or not, with the miniature supercells favored when LFC heights are low, as is often the case in landfalling tropical cyclones. This is in addition to such considerations as the shapes of the buoyancy and wind profiles (see MW01), which can also strongly influence the velocity of the updrafts and the overall severity of the storms. Such profile shape effects are readily apparent within each of Figs. 5–8.

### d. Updraft dilution

The increase in updraft overturning efficiency with increases in LFC height, evident in the CAPE-starved storms and also to a lesser degree in the shear-starved storms, suggests that storms with deep moist layers suffer less updraft thermodynamic dilution at low levels than those with low LFCs, all other things being equal. This is consistent with an analysis (Fig. 13) of the mean  $\theta_e$  within the updrafts of the mature storms as a function of altitude, for each combination of LFC and LCL heights studied in our low- $Z'_b$ , low- $Z'_v$ , variable LCL and LFC simulation series. For both the CAPE = 800 J kg<sup>-1</sup> (Fig. 13a) and 2000 J kg<sup>-1</sup> (Fig. 13b) simulations, the updrafts show smooth increasing trends in mean  $\theta_e$  as the LCL = LFC is raised, with an apparent asymptotic approach to the mean subcloud environmental  $\theta_e$  at the LFC when LCL = LFC heights reach 1.5–2.0 km. The tendency for enhancement of LFC-level updraft  $\theta_e$  is also noted in the cases where the LCL is lower than the LFC, although in those cases the low-level maximum in  $\theta_e$  tends to occupy much of the layer between the LCL and LFC. It is as though the deep convective clouds in all the simulations depicted in Fig. 13 always effec-

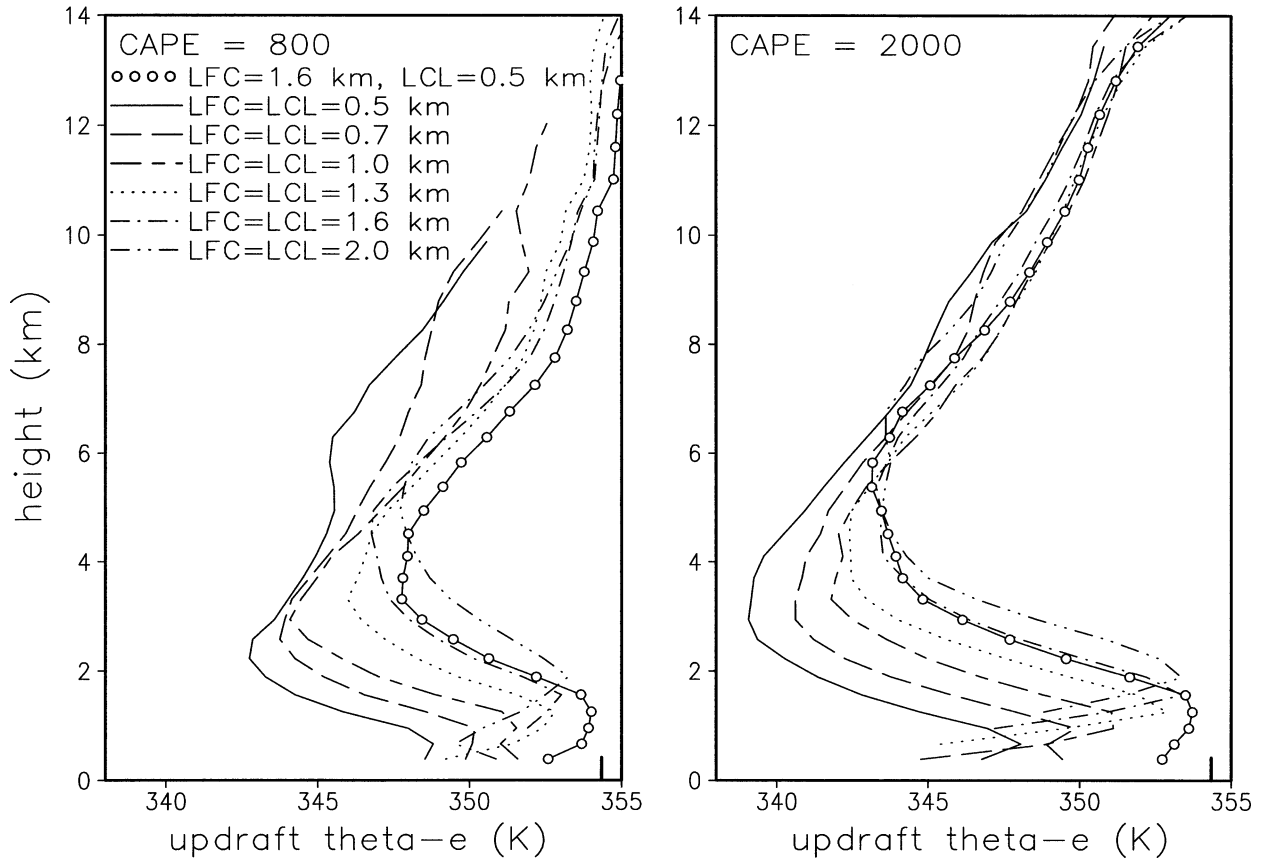


FIG. 13. Temporally averaged profiles of  $\theta_e$  within the updrafts of the principal storms in the simulation series featuring the lowest  $Z'_b$  and  $Z'_e$  from both the E0800-V12C and E2000-V12C simulations, as a function of LCL and LFC height. The curves are only drawn for layers having data points that simultaneously satisfy both of the two criteria: 1)  $w > 0.5 \text{ m s}^{-1}$ , and 2) the sum of cloud water and ice mixing ratios  $q_c + q_i > 0.01 \text{ g kg}^{-1}$ . Different combinations of LCL and LFC are drawn using individual line types, as shown on the plot legend. The small vertical tick mark at the lower right denotes the initial ambient value of  $\theta_e$  at the surface in all simulations. Note the systematic tendency for storms with high LFCs and deep sub-LFC layers of constant  $\theta_e$  to suffer less thermodynamic dilution.

tively ingest air from roughly the lowest 2 km of the troposphere, regardless of the LCL and LFC heights. Our interpretation of how this process works is as follows.

Our experiments are designed so that all environmental parcels residing beneath the LFC of surface-based air have the same initial  $\theta_e$ , and thus the same CAPE, which is equal to the MUCAPE. Thus, if downdrafts and boundary layer eddies were not present, the mean updraft  $\theta_e$  at every level below the LFC would equal that of the environment. However, downdrafts and eddies do exist and our storms pull some of the low- $\theta_e$  air that mixes down below cloud base back into their updrafts. Because of its tendency to have reduced buoyancy, this low- $\theta_e$  air is most common near the surface, and the greatest reductions in mean updraft  $\theta_e$  are seen near there, with the smallest reductions generally evident near the LFC. The deficits of LFC-level updraft mean  $\theta_e$  relative to ambient also show a systematic decrease in amplitude as the LFC altitudes increase, which suggests that contamination of LFC-level updraft air by low- $\theta_e$  air becomes less important as the LFC increases,

effectively vanishing as the LFC reaches about 2.0 km. Inspection of temporal trends in the  $\theta_e$  fields of the larger-scale environment (not shown) suggest that this contamination is regulated by both storm downdraft and ambient boundary layer mixing processes, with the latter becoming important when the LFCs are very low and low-level shears and lapse rates are strong. In the latter cases, boundary layer mixing can actually lead to gradual growth of the mixed layer depth even well away from the storms, but in our simulations this far-field growth never exceeds approximately the thickness of one model vertical grid interval. Enhanced vertical resolution sensitivity tests (not shown) indicate that the actual amount of boundary layer growth is smaller than that found in the present experiments, and apparently requires very fine low-level vertical resolution for accurate portrayal.

In summary, our high-LFC storms in Fig. 13 apparently contain higher mean  $\theta_e$  air because they ingest less of the reduced  $\theta_e$  air that originally resided just above the LFC, while our low-LFC storms ingest more of that reduced  $\theta_e$  air. The patterns in Fig. 13 thus allow us to

propose a tentative hypothesis that storms effectively ingest ambient environmental air that resides below an altitude of approximately 2 km, regardless of the LCL and LFC heights and the  $\theta_e$  profile shape below 2 km. If all the environmental air between the surface and 2 km has large  $\theta_e$ , then storm updrafts will be intense, but if the LFC exists at some altitude distinctly below 2 km, or if a layer of reduced  $\theta_e$  exists anywhere in the lowest 2 km (see also section 4e), then some reduced  $\theta_e$  air will be ingested by the updrafts, to the detriment of their intensity.

The increase in updraft overturning efficiency with increasing moist layer depth (LFC height) also occurs in conjunction with systematic changes in updraft cross-sectional area. Comparing updraft area trends in Figs. 10f and 12f with the updraft dilution trends inferred from Fig. 13, we find that the amount of updraft dilution is indeed inversely related to updraft area, as expected from continuous, homogeneous mixing theory (see, e.g., Reuter 1986 and Blyth 1993). It is not clear yet whether the reduction of updraft dilution with increasing moist layer depth is best viewed as the result of increases in updraft area, or, through mixing effects at low levels, as a cause of those increases. If the former is true, the increases in updraft area must be the result of buoyancy and shear interactions intrinsic to the structure of any given environment, and would be susceptible to analysis of the patterns of the buoyancy and perturbation pressure forcing in the lower parts of the storms. We plan to perform such analyses in the near future.

Note that our findings do not imply that storms do not mix with their environment in the layers above the LFC. The depression of updraft mean  $\theta_e$  seen throughout the midtroposphere in all the simulations is clear evidence that mixing occurs at all altitudes. Our main concern is the behavior of the mean  $\theta_e$  near the LFC, where it reaches its low-level maximum. Updrafts having larger mean  $\theta_e$  near the LFC, as seen in our high-LFC cases, simply have a "head start" with respect to buoyancy as they begin their upward journey through the midtroposphere. Despite this, updraft dilution can, of course, still vary above the LFC as a result of differences in the environmental conditions there.

It is also of interest to see how updraft dilution behaves in our other experiments, including those high-CAPE simulations that exhibit outflow dominance. To address this, we have examined the profiles of mean updraft  $\theta_e$  in all our simulations (not shown), and find no systematic environment-relative reduction in mean  $\theta_e$  at the LFC for the outflow-dominated storms that occur at  $\text{CAPE} = 2000 \text{ J kg}^{-1}$ , but some reduction at midlevels. Nearly all this updraft dilution and mean  $\theta_e$  deficit seen in the outflow-dominated storms occurs above the LFC, and is associated with the weaker shear there relative to the stronger-shear, non-outflow-dominated storms that occur in environments having similar buoyancy profiles. In fact, larger updraft mean  $\theta_e$  deficits are consistently observed at weaker shears in our shear-

starved environments, regardless of the specification of the buoyancy profile. This is apparently related to the enhancement of updraft size and organization, and attendant reduction of updraft dilution, when shear is increased in a shear-starved environment.

Figure 13 also reveals that there is a complex relationship between updraft  $\theta_e$  near the surface versus its value near the LFC, with nonmonotonic altitude dependence seen in some cases. The amount of change in updraft  $\theta_e$  between those two levels should be a function of the amount of low- $\theta_e$  downdraft air mixed down and pulled back into updrafts, and the size of the downdraft  $\theta_e$  deficit, which is here associated with its source altitude. However, updraft structural details near the surface are likely dominated by small-scale updrafts along gust fronts, especially those that are processing moist, undisturbed environmental air. We note that, despite the small, gradual drying trends seen near the surface in the smallest  $Z'_b$  and  $Z'_v$  cases, our low-LCL environments are generally characterized by higher relative humidity in the subcloud layer compared to our high-LCL cases, and are thus more likely than the latter to generate widespread cloudy updrafts along gust fronts. The curves in Fig. 13 are only drawn for layers having data points simultaneously satisfying the two criteria 1)  $w > 0.5 \text{ m s}^{-1}$ , and 2) the sum of cloud water and ice mixing ratios  $q_c + q_i > 0.01 \text{ g kg}^{-1}$ . These facts explain why some of the higher-LCL curves are not plotted near the surface, and how the subcloud  $\theta_e$  curves of other cases can sometimes be nonmonotonic.

#### e. Other sensitivity tests

For each of the initial soundings used here, the CAPE is the same for any parcel lifted from any model level below the LCL. Therefore, as the LCL varies, so does the depth of this most unstable layer. This is frequently but not always true in nature. To see what happens when the LCL is higher than the depth of the enhanced  $\theta_e$  MUCAPE layer, we designed and performed a few simulations (not shown) using soundings in which the  $\text{LCL} = \text{LFC}$  for air lifted from the surface was increased in height without increasing the depth of the MUCAPE layer, initially set at 0.5 km. This was accomplished by specifying reduced relative humidities in that portion of the subcloud layer lying above 0.5 km. In these simulations, only very weak and short-lived clouds were produced, owing to the entrainment of dry air by the parcel as it rises to its LCL. This finding is consistent with the results of Cohen (2000).

We also performed a test simulation using a modified version of the environment from the high-LFC, low-LCL case, E2000-V12C-KL2KF6. In this test, we examined the impact of reducing the environmental  $\theta_e$  in the layer between the LCL and LFC, while keeping the virtual temperature there the same as in the original simulation, so that boundary layer parcels rising through the layer would feel no buoyancy until reaching the

LFC. This was accomplished by raising the temperature slightly, while reducing the dewpoint at all points in the layer in question. As expected, because of this reduction in ambient  $\theta_e$  at low levels, the resulting storm reached an intensity that more closely resembled that from the low-LCL, low-LFC, E2000-V12C-KL2KF2 simulation. This result confirms that the moist layer effect, as seen elsewhere in this paper, is best thought of as being associated with the depth of the high  $\theta_e$  MUCAPE layer, rather than just the LFC itself.

In the present experiments that have  $LCL = LFC$ , the CIN increases slowly as the LCL is increased, but owing to the small static stability in the nearly well-mixed subcloud layer, it always remains small. Takemi (1999), in contrast, discusses the situation in which the growth of a capped boundary layer due to surface heating decreases the difference in height between the mixed layer top and the LFC, thereby eroding a more sizeable CIN. Our simulations do not necessarily apply to such a situation, and even our simulations featuring LCL heights below the LFC are designed to resemble environments where a capping inversion is removed by large-scale lifting rather than by surface heating. In general, our conclusions apply only to situations in which the LFC height is nearly the same as the top of the most unstable layer.

#### *f. Implications for severe weather*

The present findings appear to have major implications for understanding which environments can support storms capable of producing very large hail, frequent lightning, strong surface winds, and heavy precipitation. For large hail and frequent lightning, strong updrafts are required, especially aloft in the mixed-phase hydrometeor portions of the storms. Deep moist layers, at least 1.5–2.0-km thick, are helpful in maximizing updraft overturning efficiency, and appear likely to increase the chances of large hail, frequent lightning, and also heavy precipitation. However, the heavy precipitation will be subjected to considerable subcloud evaporation if the LCL is also high. This evaporation will also be accompanied by an enhanced likelihood of strong surface outflow winds.

Although a deep moist layer of the type used in these simulations tends to boost updraft overturning efficiency and overall storm intensity, its specific impact on surface vorticity is less clear. As mentioned earlier, some of our large CAPE results suggest the possibility that surface vorticity may be maximized for LFCs somewhat lower than those associated with maximum updraft strength. If the model-resolvable surface vorticity is indeed related to the probability of tornadogenesis, then it may be that, for a given LCL, tornado formation is favored when extra low-level upward buoyant accelerations associated with a relatively low LFC are present, even at the expense of peak updraft speeds aloft. Increased low-level buoyancy would also likely produce more intense

perturbation pressure minima, which could produce additional low-level stretching of vertical vorticity. These effects will be examined in more detail in the future. Detection of the effect in observations may, however, be difficult, owing to the fact that large numbers of storms would need to be sampled so that adequate controls could be placed on the other environmental parameters.

The effects of mixed and moist layer depth may have larger implications for tornadogenesis in supercells as well. Our results show that, while a high LFC is beneficial for optimizing updraft overturning efficiency, a lowered LCL reduces the strength of surface outflow, prevents outflow dominance, and promotes storm persistence, especially in shear-starved large CAPE environments. Markowski et al. (2000) have shown observational results that suggest that the absence of low- $\theta_e$  surface air within surface mesocyclones in supercells, especially in downdraft regions, tends to be associated with tornadogenesis. Storms with these favorable surface thermal characteristics appear to resemble our storms with low LCLs.

Our findings also suggest that, for the purposes of forecasting storm updraft speeds (and related severe weather manifestations such as maximum potential hail size), CAPE should be evaluated using parcels defined by mixing the lowest 2 km of the troposphere, rather than just the lowest 500 m or so as is done operationally. Although this approach seems promising for the series of storms documented in Figs. 9–13, inspection of Figs. 5–8 reveals that other environmental parameters such as the shapes of the buoyancy and shear profiles must also ultimately be taken into account when attempting to predict peak storm updraft intensity. Further research into the full parameter space affecting storms is required before general prediction equations for peak storm intensity can be developed.

#### *g. Other implications*

Our results may help explain why some convective regimes produce satellite sensor signatures suggestive of heavy surface rainfall, despite surface rain gauges collecting lesser rainfall. In the highlands of central tropical Africa, for example, intense convective storms are often indicated by satellite sensors and lightning observing systems (see, e.g., Boccippio et al. 2000), but surface rainfall is found to be less than anticipated (McCollum et al. 2000). We believe these observations can be reconciled by our present data, wherein it is found that storms with relatively deep subcloud mixed layers tend to have high overturning efficiency, but suffer considerable evaporation of their rain in the deep, well-mixed subcloud layer. All other things being equal, such storms would look intense in satellite imagery, but would show less surface rainfall than expected for storms of that apparent intensity. They would also be vulnerable to outflow dominance, and in the absence of

any imposed larger-scale organization, would tend to be short-lived. The mechanism of enhanced subcloud rain evaporation is one of the explanations advanced by McCollum et al. (2000), but embraced somewhat hesitantly, perhaps because of lack of awareness of the beneficial effects on updraft overturning efficiency of a high LFC supported by a deep, well-mixed subcloud layer.

Our results also point to yet another reason why many maritime convective storms forming in the Tropics underachieve with respect to updraft strength and overturning efficiency (see, e.g., Lucas et al. 1994): Not only are their buoyancy profile shapes not optimized for efficient overturning (see MW01 and our Figs. 5 and 7), owing to their typically high altitudes of maximum buoyancy, but their LFCs are also too close to the surface. This does not, however, imply that low-LFC storms can never be intense enough to be classified as severe; storms developing within landfalling tropical cyclones routinely have low LFCs and become severe enough to produce tornadoes (see e.g., McCaul 1991, 1993). It does, however, suggest that such storms might have had even larger overturning efficiencies and might have been even more severe in many respects had their LFCs been higher, all other things being equal.

#### *h. Comparison with observations*

Our simulation results appear to be consistent with many of the general findings of extant rawinsonde-based climatologies of severe storms (see, e.g., Bluestein and Parks 1983; Bluestein and Jain 1985; Rasmussen and Straka 1998; Rasmussen and Blanchard 1998). From these studies, the consensus seems to be that the mean LFC heights in severe storm events are generally near 2 km, which is close to optimal for updraft overturning efficiency according to our simulation results. The climatologies also show typical LCL heights roughly near 1.5 km, which is almost 0.5 km lower than the LFC height and therefore at least somewhat beneficial in reducing the tendency for storms to become outflow-dominated.

In addition, Rasmussen and Blanchard (1998) found that, for storms producing large (at least 5-cm wide) hail only, without at least F2 strength tornadoes, the LCL heights were significantly higher than for ordinary thunderstorms. LFC statistics were not available. Caution is required, however, when interpreting the statistics presented in all the rawinsonde-based climatology studies. This is because no attempt was made in them to group soundings into classes having approximately similar values of key sounding parameters, so that meaningful inferences regarding the influence of any given key parameter could be drawn by comparing groups of events spanning different classes of the given parameter, but occupying similar classes for all other key parameters. Thus, findings of a negative correlation between bulk CAPE and vertical shear in severe storm cases may

be nothing more than an artifact of the negative correlation that likely exists between those two parameters throughout the atmosphere as a whole. We propose that more insight would be obtained into the physics of storms if paired statistics of environmental parameters were reexamined using only sets of soundings carefully controlled for the values of all other key sounding parameters.

#### *i. The convective parameter space*

Of course, part of the problem with conducting statistically rigorous observational studies of storm morphology and intensity is in knowing exactly which parameters of an environmental sounding are indeed key to explaining variations among storms. All investigators who have attempted to confront this problem have come to appreciate the tremendous diversity of conditions that may be observed in the atmosphere. Still, it is of interest to seek to reduce the true complexity of the problem to some simplified form, using a framework that supports most of that complexity without admitting intractability. We believe the simulation design framework reported and used here and in MW01 can be considered a step towards that goal.

In our approach, we have restricted study only to those “well-behaved” environments having reasonably smooth profiles and negligible convective inhibition—just the kind of environments most amenable to study with numerical simulation techniques. For these cases, the MW01 approach to specifying the environmental profiles appears to be flexible enough to permit reconstruction of the essential thermodynamic features of any smooth storm sounding, and thus also to serve as a basis for identifying the key thermodynamic parameters of soundings. Defining the key kinematic parameters of sounding wind profiles is more challenging, because of the prodigious variety of possible wind component profile shapes and amplitudes; however, the MW01 approach handles simple versions of the straight and curved hodograph archetypes adequately, at least for those often-observed cases where vertical shear is stronger near the surface than aloft.

Subject to the foregoing constraints, the key thermodynamic parameters of a storm environment may be said to be the free parameters that must be specified in order to construct a sounding’s thermodynamic profiles using the approach of MW01. These parameters are: bulk CAPE, level of maximum buoyancy (or the shape parameter for the buoyancy profile), LCL altitude for subcloud air (our proxy for mixed layer depth), LFC altitude (our proxy for moist layer depth), subcloud  $\theta_e$  (or, alternatively, either temperature or water vapor mixing ratio at the LCL), and the shape parameter for the relative humidity profile above the LFC. Because column-integrated water vapor [precipitable water (PW)] in storm environments is strongly dominated by the amounts present in the lower troposphere, PW may be

said to serve as a rough proxy for subcloud  $\theta_e$ . Strictly speaking, tropopause height and stratospheric static stability are additional parameters, although they are assumed to be constant in the method of MW01 and in the present study, and are probably of secondary importance. Thus, neglecting tropopause-structure variability and assuming negligible convective inhibition, the number of key thermodynamic parameters reduces to six. Under the simplified wind profile regimes of MW01, both curved and straight wind hodographs are described using two parameters, hodograph radius or equivalent radius, and wind profile shape parameter. Thus, a minimum of eight key parameters are needed to describe the basic characteristics of a simple sounding.

In this study and in MW01, exploratory simulation studies have already been made for six of these: bulk CAPE, bulk shear (hodograph trace), the shapes of both the buoyancy and shear profiles, and LCL and LFC altitudes. Earlier work by Weisman and Klemp (1982, 1984) also explored the bulk CAPE and bulk shear components of this parameter space, but without independent controls on the shapes of the buoyancy and shear profiles and on LCL and LFC altitudes. The work of Gilmore and Wicker (1998) dealt with a seventh key parameter, the shape of the relative humidity profile, although they studied its impact on storms using a different sounding design framework than that employed here. They found increased midtropospheric dryness and the attendant reduction of environmental midlevel  $\theta_e$  enhanced a storm's susceptibility to outflow dominance. Rasmussen and Straka (1998) also found observational evidence that heavy-precipitation supercells, which, according to the data presented in MW01, occupy that part of the supercell spectrum closest to outflow dominance and multicell transition, are favored in environments having very dry midtropospheric air.

Finally, it should be noted that the present experiments were designed to explore questions of basic storm physics within carefully specified, idealized, horizontally homogeneous environments, and the conclusions regarding the impacts of mixed and moist layer depth apply only when all other key sounding parameters are held fixed. Furthermore, it is important to remember that the LCL heights discussed in this paper are those calculated from the undisturbed storm environment, and are not always representative of actual observed cloud-base heights in the disturbed environment beneath storms. We also emphasize that, while our high-LFC storms show generally larger updraft overturning efficiencies than our low-LFC storms, other factors can and do affect these efficiencies. We have not, for instance, addressed the issue of storm interactions and their effect on the morphology of storms and storm systems, even though it is known (see, e.g., Bluestein and Weisman 2000) that convective line organization can be strongly affected by the orientation of the mean vertical shear with respect to the line along which the convection is

being triggered. It is precisely the large size of the relevant parameter space and the wealth of environmental permutations that make understanding convective storm morphology so challenging.

## 5. Summary and future outlook

In this paper, we use a cloud model containing ice physics to confirm and extend the MW01 findings regarding the importance of the shapes of buoyancy and shear profiles for storm morphology and intensity, and demonstrate further that the depths of the mixed and moist layers are additional major independent determinants of storm structure and intensity. In particular, we find storm convective overturning efficiency is maximized for moist layer depths of at least 1.5–2.0 km, with the tendency for outflow dominance being enhanced when mixed layer depths are high, but suppressed when they are low. Storm morphology and intensity are found to exhibit different sensitivities to key environmental parameters, depending on the degree of CAPE- or shear-starvation characterizing the storm environment. We find, for instance, that some storms in CAPE = 800 J kg<sup>-1</sup> environments having favorable buoyancy and shear profile shapes and mixed and moist layer depths can actually be more intense than those in CAPE = 2000 J kg<sup>-1</sup> environments having unfavorable combinations of those parameters.

We emphasize that the present findings are exploratory and may not describe all the important features that might be found in a more exhaustive parameter space study. In the future, this research should be expanded to include more classes of bulk CAPE, bulk shear, and shear profile shape, and additional choices of LCL altitude beneath the LFC. The impact on storms of independent variation of environmental precipitable water should also be examined, as should the effect of varying reductions in  $\theta_e$  in the layer between the LCL and LFC, when the two altitudes are different. The impacts on storm motion of LFC and LCL height changes, and also of buoyancy and shear profile changes (see MW01), should also be reassessed for these ice-physics simulations. The sensitivity of storm and storm system morphology to the key environmental sounding parameters discussed here under quasi-linear rather than circular triggering disturbances also requires investigation, and is being pursued elsewhere at the time of this writing (J. Trapp, NCAR, 2001, personal communication). In addition, it is clear that there is a need to develop quantitative, objective measures of storm morphology, based preferably on some combination of the most sensitive radar-observable variables. This would facilitate progress in comparing aspects of observed and simulated storms, help clarify the strengths and shortcomings of both approaches, and ultimately lead to improved understanding of storm behavior and better severe weather forecasts.

As suggested by MW01, heat and momentum budget

studies (Lilly and Jewett 1990) should also be conducted, to see how storm dynamics respond to changes in the key environmental parameters. Finer-resolution simulations should also be performed to see if the key environmental parameters exert any significant influence on vorticity development at tornado scales, and to define more precisely the details of how convection behaves in environments having very small LCL and LFC heights. Finally, additional comprehensive sounding-based statistical climatologies should be developed using data classifications based on distinct ranges of values of the key environmental parameters, in order to help clarify how storms actually respond to changes in individual parameters, and to determine just how often the real atmosphere visits each part of the multidimensional parameter space.

*Acknowledgments.* This research has been supported by the NASA Earth Science Enterprise under the Mesoscale Atmospheric Processes Program and by the Earth Observing System Interdisciplinary Science Program and administered through Cooperative Agreement NCC8-142 between NASA Marshall Space Flight Center and the Universities Space Research Association. The RAMS simulations were conducted on Cray J90 and SGI workstations at Marshall Space Flight Center in Huntsville, Alabama. We thank colleagues Morris Weisman and Jeff Trapp (NCAR), Kevin Knupp (UAH), Steve Goodman (NASA MSFC), and Don Burgess and Lou Wicker (NSSL), for their interest in this work. We are also grateful to anonymous reviewers, who provided a number of insightful and constructive comments that led to improvements in the manuscript.

#### REFERENCES

- Auer, A. H., Jr., and D. L. Veal, 1970: The dimension of ice crystals in natural clouds. *J. Atmos. Sci.*, **27**, 919–926.
- Bluestein, H. B., and C. R. Parks, 1983: A synoptic and photographic climatology of low-precipitation severe thunderstorms in the southern plains. *Mon. Wea. Rev.*, **111**, 2034–2046.
- , and M. H. Jain, 1985: Formation of mesoscale lines of precipitation: Severe squall lines in Oklahoma during the spring. *J. Atmos. Sci.*, **42**, 1711–1732.
- , and M. L. Weisman, 2000: The interaction of numerically simulated supercells initiated along lines. *Mon. Wea. Rev.*, **128**, 3128–3149.
- Blyth, A. M., 1993: Entrainment in cumulus clouds. *J. Appl. Meteor.*, **32**, 626–641.
- Boccippio, D. J., S. J. Goodman, and S. Heckman, 2000: Regional differences in tropical lightning distributions. *J. Appl. Meteor.*, **39**, 2231–2248.
- Braham, R. R., Jr., 1952: The water and energy budgets of the thunderstorm and their relationship to thunderstorm development. *J. Meteor.*, **9**, 227–242.
- Brooks, H. E., C. A. Doswell III, and J. Cooper, 1994a: On the environments of tornadic and nontornadic mesocyclones. *Wea. Forecasting*, **9**, 606–618.
- , —, and R. B. Wilhelmson, 1994b: The role of midtropospheric winds in the evolution and maintenance of low-level mesocyclones. *Mon. Wea. Rev.*, **122**, 126–136.
- Cohen, C., 2000: A quantitative investigation of entrainment and detrainment in numerically simulated cumulonimbus clouds. *J. Atmos. Sci.*, **57**, 1657–1674.
- Fujita, T., 1959: Precipitation and cold air production in mesoscale thunderstorm system. *J. Meteor.*, **16**, 454–466.
- Gilmore, M. S., and L. J. Wicker, 1998: The influence of midtropospheric dryness on supercell morphology and evolution. *Mon. Wea. Rev.*, **126**, 943–958.
- Klemp, J. B., and R. B. Wilhelmson, 1978: The simulation of three-dimensional convective storm dynamics. *J. Atmos. Sci.*, **35**, 1070–1096.
- Lilly, D. K., 1962: On the numerical simulation of buoyant convection. *Tellus*, **14**, 148–172.
- , and B. F. Jewett, 1990: Momentum and kinetic energy budgets of simulated supercell thunderstorms. *J. Atmos. Sci.*, **47**, 707–726.
- Lucas, C., E. J. Zipser, and M. A. LeMone, 1994: Vertical velocity in oceanic convection off tropical Australia. *J. Atmos. Sci.*, **51**, 3183–3193.
- Markowski, P., E. Rasmussen, and J. Straka, 2000: Surface thermodynamic characteristics of RFDs as measured by a mobile mesonet. Preprints, *20th Conf. on Severe Local Storms*, Orlando, FL, Amer. Meteor. Soc., 251–254.
- McCaul, E. W., Jr., 1991: Buoyancy and shear characteristics of hurricane tornado environments. *Mon. Wea. Rev.*, **119**, 1954–1978.
- , 1993: Observations and simulations of hurricane-spawned tornadic storms. *The Tornado: Its Structure, Dynamics, Prediction, and Hazards*, C. R. Church, Ed., Amer. Geophys. Union, 119–142.
- , and M. L. Weisman, 1996: Simulations of shallow supercell storms in landfalling hurricane environments. *Mon. Wea. Rev.*, **124**, 408–429.
- , and —, 2001: The sensitivity of simulated supercell structure and intensity to variations in the shapes of environmental buoyancy and shear profiles. *Mon. Wea. Rev.*, **129**, 664–687.
- McCollum, J. R., A. Gruber, and M. B. Ba, 2000: Discrepancy between gauges and satellite estimates of rainfall in equatorial Africa. *J. Appl. Meteor.*, **39**, 666–679.
- Pielke, R. A., and Coauthors, 1992: A comprehensive meteorological modeling system—RAMS. *Meteor. Atmos. Phys.*, **49**, 69–91.
- Rasmussen, E. N., and D. O. Blanchard, 1998: A baseline climatology of sounding-derived supercell and tornado forecasting parameters. *Wea. Forecasting*, **13**, 1148–1164.
- , and J. M. Straka, 1998: Variations in supercell structure. Part I: Observations of the role of upper-level storm-relative flow. *Mon. Wea. Rev.*, **126**, 2406–2421.
- Reuter, G. W., 1986: A historical review of cumulus entrainment studies. *Bull. Amer. Meteor. Soc.*, **67**, 151–154.
- Smagorinsky, J., 1963: General circulation experiments with the primitive equations. Part I: The basic experiment. *Mon. Wea. Rev.*, **91**, 99–164.
- Starr, D. O'C., and S. K. Cox, 1985: Cirrus clouds. Part I: A cirrus cloud model. *J. Atmos. Sci.*, **42**, 2663–2681.
- Takemi, T., 1999: Structure and evolution of a severe squall line over the arid region in northwest China. *Mon. Wea. Rev.*, **127**, 1301–1309.
- Tripoli, G. J., and W. R. Cotton, 1982: The Colorado State University three-dimensional cloud/mesoscale model—1982. Part I: General theoretical framework and sensitivity experiments. *J. Rech. Atmos.*, **16**, 185–219.
- Walko, R. L., W. R. Cotton, M. P. Meyers, and J. Y. Harrington, 1995: New RAMS cloud microphysics parameterization. Part I: The single-moment scheme. *Atmos. Res.*, **38**, 29–62.
- Weisman, M. L., and J. B. Klemp, 1982: The dependence of numerically simulated convective storms on vertical wind shear and buoyancy. *Mon. Wea. Rev.*, **110**, 504–520.
- , and —, 1984: The structure and classification of numerically simulated convective storms in directionally varying shears. *Mon. Wea. Rev.*, **112**, 2479–2498.